DEVELOPMENT AND VALIDATION OF TEST RIG FOR MEASUREMENTS OF LEAKAGE AND ROTORDYNAMIC PERFORMANCE OF INTERLOCKING GAS LABYRINTH SEALS

A Thesis

by

MAURICIO ALAN RAMIREZ ALANIS

Submitted to the Office of Graduate and Professional Studies of
Texas A&M University
in partial fulfillment of the requirements for the degree of

MASTER OF SCIENCE

Chair of Committee,	Dara W. Childs
Committee Members,	Luis San Andres
	Ray James
Head of Department,	Andreas Polycarpou

December 2017

Major Subject: Mechanical Engineering

ABSTRACT

Understanding the rotordynamic and leakage characteristics of gas annular seals is important for the design of efficient and reliable turbomachinery. This work sets the foundation to advance the understanding of gas interlocking labyrinth seals. Data for such seals are vague and scarce in literature. A test rig for interlocking seals is developed and validated via tests for a see-through tooth-on-stator labyrinth seal. Test procedures by Millsaps in 1994 and Wagner et al. in 2009 are adapted. Dynamic forces are integrated from the perturbed pressure fields created inside the seal cavities while precessing the rotor using magnetic bearings. Measurements are made by adapting a test rig at the Turbomachinery Lab at Texas A&M University, previously used in 2006 for a different purpose. The see-through seal has eight stator teeth and a smooth rotor. The rotor has a 75 mm radius, 3 mm tooth height, and 0.2 mm radial clearance. Tests at a rotor speed of 10 kRPM are performed for a range of inlet pressures, pressure ratios, and precession frequencies between 15 and 50 Hz. Forward and backward precessions are imposed. Measured leakage values and rotordynamic coefficients validate the performance of the test rig.

Experience showed that differential pressure transducers, a well-machined stator, and precise centering and alignment are required for correct measurements. Two sensors 180° apart from each other in a representative cavity demonstrate the development of a theoretically correct pressure wave inside the seal. All results are repeatable. Static pressure measurements in the seal cavities show pressure dropping linearly across the seal's cavities. Results show frequency-independent rotordynamic coefficients.

As noted above, only one of the seal's cavities was provided with dynamic pressure measurements, and the following rotordynamic coefficients apply for that cavity, not the entire seal. Measured negative values of direct stiffness K and cross-coupled damping c confirm the lagging pressure wave is behind the rotor, pushing it radially towards the stator. Positive values of cross-coupled stiffness k and direct damping C counteract each other in the circumferential direction, the former being

destabilizing. Effective damping C_{eff} combines the impact of direct damping C and cross-coupled stiffness k. For the cavity chosen, C_{eff} values are negative, and thus destabilizing in the circumferential direction.

Future work involves testing interlocking labyrinth seals and using the test results to benchmark CFD codes.

DEDICATION

To my parents for their love and sacrifice.

ACKNOWLEDGEMENTS

I am extremely grateful for the opportunity to work under the supervision of Dr. Dara Childs. The support and confidence he bestowed on me became essential in the completion of this project and in my development as an engineer. His amiability and kindness turned a very challenging project into an enjoyable graduate school experience.

I would like to thank Professors Luis San Andrés, and Ray James for kindly serving as committee members and helping in the preparation of this thesis.

I would like to express appreciation to Doosan Škoda Power for sponsoring the master's research project on this test rig. Its realization was at all times graciously supported by Zdeněk Kubin, and Dan Hasnedl.

Special thanks to Mr. Stephen Phillips for his guidance throughout the project. His insights became key in the design, troubleshooting, and implementation of the test rig. And to Mr. Ray Mathews for assisting with the tools and workspace required on a daily basis.

Many thanks to my friend and colleague Andrew Crandall for his selfless help throughout the project, especially in the implementation of a data acquisition system.

Sincere thanks to Daren Tremaine of SKF, Dr. Eric Maslen of James Madison University, Dr. Alan Palazzolo of Texas A&M University, and former Turbomachinery Lab Research Assistant Rasish Khatri for assisting with the magnetic bearings.

I am very fortunate to have shared time working on the test rig with Tanja Baumann and Keith Gary, both incredibly smart, hardworking, and fun to be around.

I would like to thank my many friends at the Turbomachinery Lab for making every day enjoyable. David Coghlan and Stephen Arthur for introducing me to the lab as an undergratduate assistant. My office mates: Travis Cable, Michael Rohmer, and Scott Wilkinson and undergraduate assistants: Michael Alvarez, and Nicholas Niemiec.

Finally, I would like to thank my parents and siblings for their infinite support.

CONTRIBUTORS AND FUNDING SOURCES

Contributors

This work was supported by a thesis committee consisting of Professors Dara Childs [advisor] and Luis San Andres of the Department of Mechanical Engineering and Professor Ray James of the Department of Civil Engineering.

The data in Figure 32 was provided by colleague Xueliang Lu. Andrew Crandall and Keith Gary provided extensive support in the development of a data acquisition system and alignment methods.

Funding Sources

This study was financed by Doosan Skoda Power through TEES.

NOMENCLATURE

c	Cross-coupled damping [FT/L]
C	Direct damping [FT/L]
e_0	Precession eccentricity [L]
F	Force [F]
k	Cross-coupled stiffness [F/L]
K	Direct stiffness [F/L]
P	Peak precessing cavity pressure [F/L^2]
R	Seal radius [L]
V	Air Velocity [L/T]
β	Phase reference between position and pressure, introduced in Fig. 6
ρ	Density [M/L^3]
ω	Rotor speed [1/T]
Ω	Precession frequency [1/T]
C_{eff}	Effective Damping, defined in Eq. 4 [FT/L]
K_{eff}	Effective Stiffness, defined in Eq. 6 [F/L]
L_C	Length of cavity between labyrinth teeth, seen in Fig. 17 [L]
P_d	Dynamic pressure [F/L^2]
P_S	Static pressure [F/L^2]
P_T	Total pressure [F/L^2]
ΔP	Differential pressure [F/L^2]

Subscripts

r	Radial direction
θ	Circumferential direction
3	Third labyrinth seal cavity

Superscripts

+	Forward precession
-	Backward precession

Acronyms

DE	Drive End
NDE	Non-Drive End
PSR	Pre-Swirl Ratio
TOR	Tooth-On-Rotor
TOS	Tooth-On-Stator
WFR	Whirl Frequency Ratio

TABLE OF CONTENTS

Page

ABSTRACT ii

DEDICATION iv

ACKNOWLEDGEMENTS v

CONTRIBUTORS AND FUNDING SOURCES vi

NOMENCLATURE vii

LIST OF FIGURES xi

LIST OF TABLES xvi

1. INTRODUCTION 1

2. PROCEDURE 9

3. TEST APPARATUS 14

- 3.1 Swirl Vane 17
- 3.2 Swirl Brakes 18
- 3.3 Test Seals 19
- 3.4 Instrumentation 20
- 3.5 Pressure Drop 25
- 3.6 Leakage 27
- 3.7 Alignment 27
- 3.8 Magnetic Bearings 29
- 3.9 Uncertainty 30
- 3.10 DAQ 31
- 3.11 LabView 32
- 3.12 Repeatability 35
- 3.13 Test Matrix 36

4. DISCUSSION OF RESULTS 38

- 4.1 Static Results 38
- 4.2 Dynamic Forces 42

5. DYNAMIC RESULTS 49
6. SUMMARY AND CONCLUSIONS.....70
REFERENCES.....71
APPENDIX A DYNAMIC FORCE EQUATIONS BY CHILDS 73
APPENDIX B STATIC RESULTS AT 0 RPM. 75
APPENDIX C DYNAMIC RESULTS AT 0 RPM. 77
APPENDIX D DYNAMIC MEASUREMENTS 80

LIST OF FIGURES

Page

Figure 1. Annular gas seal locations in the final stages of a straight-through centrifugal compressor [1].....2

Figure 2. Cross section schematic of tooth-on-rotor (A), tooth-on-stator (B), and interlocking (C) labyrinth seal configurations. 2

Figure 3. Dynamic model of a gas labyrinth seal with a centered rotor [6]. 4

Figure 4. Direct and cross-coupled seal reaction forces acting on a forward precessing rotor. 5

Figure 5. Direct and cross-coupled seal reaction forces acting on a backward precessing rotor. 6

Figure 6. Schematic of reaction forces in the seal due to the rotor's displacement. 9

Figure 7. Measurements of circumferential force as a function of precession frequency for single gland TOR seals by Millsaps [10]. 11

Figure 8. Predicted normalized radial (A) and circumferential (B) forces. 12

Figure 9. Test rig used by Zachary Zutavern for doctoral dissertation in 2006 [13]. 15

Figure 10. Components of test section. 16

Figure 11. CAD model of (A) fully assembled test rig, and (B) an exploded view of the test rig showing the top and bottom stator halves [14]. 17

Figure 12. Swirl vane design with Pitot tube location. 18

Figure 13. Front view of spacer ring (A) and swirl brake (B) possible options. 19

Figure 14. TOS seal drawings in mm. 19

Figure 15. Smooth seal rotor shrunk onto shaft drawings with units of mm 20

Figure 16. Schematic of diaphragm inside of differential pressure transducer with a balanced (A), positive (B), and negative (C) net pressure. 21

Figure 17. Differential pressure transducer and plenum installation in test section. 22

Figure 18. Schematic of labyrinth seal cross section. 23

Figure 19. Pressure and position probe placement seen from the front of the NDE bearing. 24

Figure 20. Front and side view of exit labyrinth seal with three teeth and a ~10 mm land for rotor support in case of contact. 26

Figure 21. Back pressure control valve and exhaust hoses. 27

Figure 22. Mandrel used to align all parts of the top and bottom stator. 28

Figure 23. Stator full assembly. 29

Figure 24. Bump test calibration of YDE axis, 0.15 mm radial clearance. 30

Figure 25. Injecting precession signals using module NI 9263. 32

Figure 26. Excitation VI (left) used to precess the rotor at 40 Hz as seen in the Input VI (right). 33

Figure 27. Roundness of forward precession orbit measured using the XDE phase as reference. 34

Figure 28. Roundness of backward precession orbit measured using the XDE phase as reference. 34

Figure 29. Monitoring tools and Input VI used while testing at 7.5 kRPM. 35

Figure 30. PSR measurements for range of inlet pressures tested at 0 and 10 kRPM. 40

Figure 31. Mass flow rate vs Pressure Ratio. 41

Figure 32. Measured and predicted mass flow rate vs Pressure Ratio at 10 kRPM. 42

Figure 33. Radius of precession eccentricity e_0. 43

Figure 34. Position and pressure measurements vs time for 30 Hz precession at 3.79 bar inlet pressure and 0.7 pressure ratio. 44

Figure 35. Frequency response position measurements for all axes for a 50 Hz precession at 3.79 bar inlet pressure and 0.7 pressure ratio. 45

Figure 36. Frequency response of dynamic pressure sensor 6 for a 50 Hz precession at 3.79 bar inlet pressure and 0.7 pressure ratio 46

Figure 37. Coherence plot of output pressure due to an input displacement for a 50 Hz precession at 3.79 bar inlet pressure and 0.7 pressure ratio..... 47

Figure 38. Pressure drop across labyrinth seal cavities for a (A) 2.76, (B) 3.79, and (C) 4.83 bar inlet pressure at 10 kRPM. 48

Figure 39. Measured (A) F_{r3}/e_0 , (B) $F_{\theta 3}/e_0$, (C) β, and (D) P_3 for forward precession at 3.79 bar inlet pressure and 0.7 pressure ratio. 50

Figure 40. Measured (A) $F_{\theta 3}/e_0$, (B) $F_{\theta 3}/e_0$, (C) β, and (D) P_3 for backward precession at 3.79 bar inlet pressure and 0.7 pressure ratio..... 51

Figure 41. $F_{\theta 3}/e_0$ versus Ω for a (A) 2.76, (B) 3.79, and (C) 4.83 bar inlet pressure, and four pressure ratios at 10 kRPM..... 53

Figure 42. $F_{\theta 3}/e_0$ versus Ω, for a (A) 2.76, (B) 3.79, and (C) 4.83 bar inlet pressure, and four pressure ratios at 10 kRPM. 55

Figure 43. *K* versus Ω for third cavity for a (A) 2.76, (B) 3.79, and (C) 4.83 bar inlet pressure and four pressure ratios at 10 kRPM. 58

Figure 44. *C* versus Ω for third cavity for a (A) 2.76, (B) 3.79, and (C) 4.83 bar inlet pressure and four pressure ratios at 10 kRPM. 60

Figure 45. *k* versus Ω for third cavity for a (A) 2.76, (B) 3.79, and (C) 4.83 bar inlet pressure and four pressure ratios at 10 kRPM. 61

Figure 46. *c* versus Ω for third cavity for a (A) 2.76, (B) 3.79, and (C) 4.83 bar inlet pressure and four pressure ratios at 10 kRPM. 63

Figure 47. K_{eff} versus Ω for third cavity for a (A) 2.76, (B) 3.79, and (C) 4.83 bar inlet pressure and four pressure ratios at 10 kRPM. 65

Figure 48. C_{eff} versus Ω for third cavity for a (A) 2.76, (B) 3.79, and (C) 4.83 bar inlet pressure and four pressure ratios at 10 kRPM. 67

Figure 49. *WFR* versus Ω for third cavity for a (A) 2.76, (B) 3.79, and (C) 4.83 bar inlet pressure and four pressure ratios at 10 kRPM. 69

Figure B - 1. Pressure drop across cavities for a (A) 2.76, (B) 3.79, and (C) 4.83 bar inlet pressure at 0 RPM. 76

Figure B - 2. $F_{\theta 3}/e_0$ versus Ω for a (A) 2.76, (B) 3.79, and (C) 4.83 bar inlet pressure at 0 RPM. 77

Figure B - 3. F_{r3}/e_0 versus **Ω** for a (A) 2.76, (B) 3.79, and (C) 4.83 bar inlet pressure at 0 RPM. 78

Figure D - 1 Phase β and pressure P of third cavity for 2.76 bar pressure drop at 0.5 PR. 80

Figure D - 2 Phase β and pressure P of third cavity for 2.76 bar pressure drop at 0.6 PR. 80

Figure D - 3 Phase β and pressure P of third cavity for 2.76 bar pressure drop at 0.7 PR. 81

Figure D - 4 Phase β and pressure P of third cavity for 2.76 bar pressure drop at 0.8 PR. 81

Figure D - 5 Phase β and pressure P of third cavity for 3.79 bar pressure drop at 0.5 PR. 82

Figure D - 6 Phase β and pressure P of third cavity for 3.79 bar pressure drop at 0.6 PR. 82

Figure D - 7 Phase β and pressure P of third cavity for 3.79 bar pressure drop at 0.7 PR. 83

Figure D - 8 Phase β and pressure P of third cavity for 3.79 bar pressure drop at 0.8 PR. 83

Figure D - 9 Phase β and pressure P of third cavity for 4.83 bar pressure drop at 0.5 PR. 84

Figure D - 10 Phase β and pressure P of third cavity for 4.83 bar pressure drop at 0.6 PR. 84

Figure D - 11 Phase β and pressure P of third cavity for 4.83 bar pressure drop at 0.7 PR. 85

Figure D - 12 Phase β and pressure P of third cavity for 4.83 bar pressure drop at 0.8 PR. 85

LIST OF TABLES

Page

Table 1. Sensors used during tests. 25

Table 2. TOS labyrinth seal testing conditions. 37

Table 3. Static pressure measurements for tests at 10 kRPM. 39

Table 4. Rotordynamic coefficients and R^2 values for linear regressions for third cavity. 56

1. INTRODUCTION

Turbomachinery refers to machines that transfer energy between a fluid and a rotor, such as turbines, compressors, and pumps. Leakage of the working fluid through annular seals reduces the efficiency of turbomachines. Leakage is inevitable due to differences in fluid pressure and the clearances between stationary and rotating components. Labyrinth seals are types of annular seals that force the fluid through a tortuous path to effectively reduce leakage. Figure 1 shows the last two stages of a centrifugal straight-through compressor. The impellers rotate with the rotor to pressurize the fluid. Eye-packing seals reduce leakage between the stator and impeller, while shaft seals reduce leakage between the rotor and the stator from one stage to the previous. In this example, both eye-packing and shaft seals are labyrinth tooth-on-stator (*TOS*) seals having stationary teeth facing a smooth rotor. Tooth-on-rotor (*TOR*) labyrinth seals are commonly used in turbines. The balance piston seal at the end of the straight-through compressor attempts to seal the largest pressure difference in the compressor. The figure shows an interlocking labyrinth balance piston seal, in which a tooth on rotor is followed by one on the stator forming a cavity, then again on the rotor, and so on.

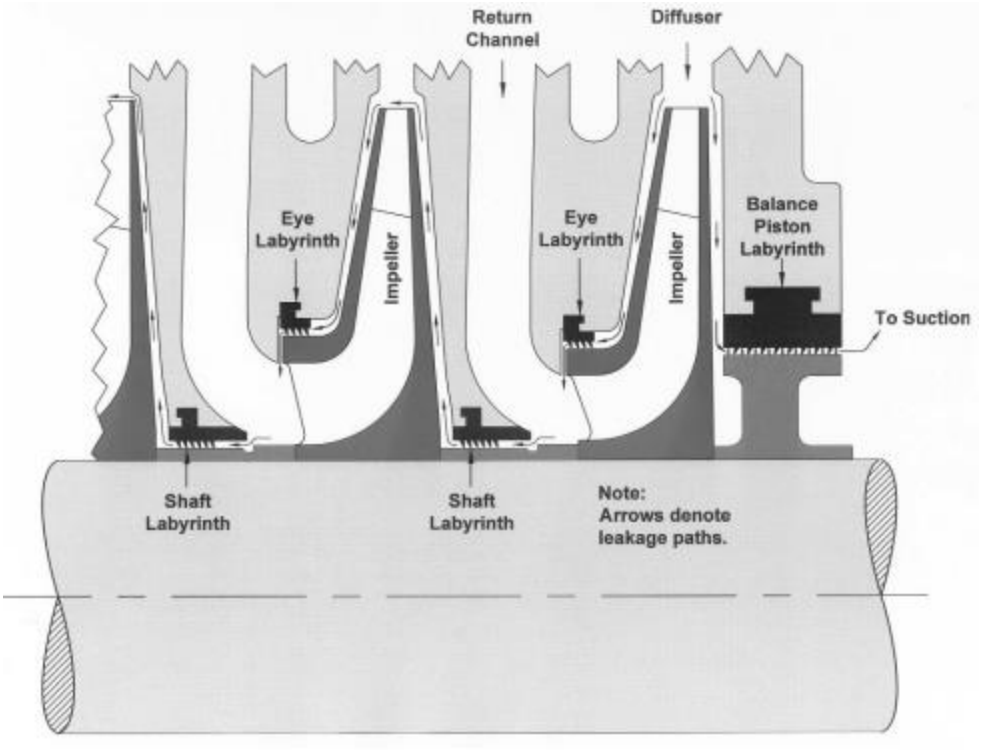

Figure 1. Annular gas seal locations in the final stages of a straight-through centrifugal compressor. Reprinted from [1].

This study focuses on labyrinth seals. Sketches (A) and (B) in Fig. 2 are see-through labyrinth seals with *TOR* and *TOS* respectively, whereas (C) depicts an interlocking labyrinth seal. The radial clearance is the minimum distance between the stator and rotor. Gas seals commonly have clearance-to-radius ratios of ~0.2% [2].

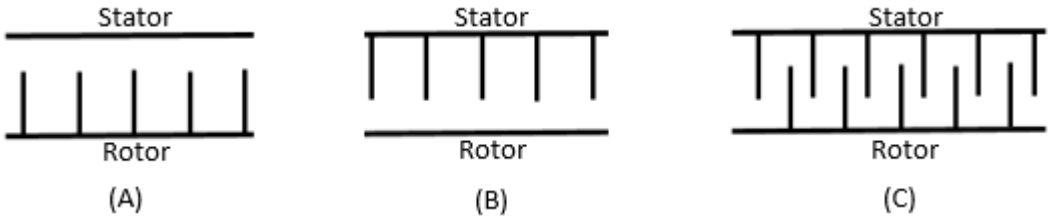

Figure 2. Cross section schematic of tooth-on-rotor (A), tooth-on-stator (B), and interlocking (C) labyrinth seal configurations.

Radial vibration in the rotor creates reaction forces in the seal cavities that impact the dynamics of a rotor-bearing system. Knowing the seal's rotordynamic and leakage characteristics is important for the design of efficient and reliable turbomachinery. Rotordynamic computer models anchored to test results exist for see-through labyrinth seals [3, 4], but measurements are scarce, and models have not been published for interlocking labyrinth seals. This study presents the development of a test rig capable of measuring rotodynamic performance of interlocking seals. Measurements of a see-through *TOS* labyrinth seal validate the functionality and accuracy of the test rig.

Figure 3 shows a rotor that is centered in a labyrinth seal with an exaggerated clearance where *x* and *y* are orthogonal axes. Childs [5] describes the reaction forces of a labyrinth seal to a displaced rotor as a combination of linear stiffness and damping coefficients

$$-\begin{Bmatrix} f_{seal_x} \\ f_{seal_y} \end{Bmatrix} = \begin{bmatrix} K_{xx} & K_{xy} \\ K_{yx} & K_{yy} \end{bmatrix} \begin{Bmatrix} x \\ y \end{Bmatrix} + \begin{bmatrix} C_{xx} & C_{xy} \\ C_{yx} & C_{yy} \end{bmatrix} \begin{Bmatrix} \dot{x} \\ \dot{y} \end{Bmatrix} \quad (1)$$

f_{seal_x} and f_{seal_y} are the seal reaction forces, K_{xx} and K_{yy} are direct stiffness, K_{xy} and K_{yx} the cross-coupled stiffness, C_{xx} and C_{yy} direct damping, C_{xy} and C_{yx} represent cross-coupled damping. Together, these are known as rotordynamic coefficients. Position and velocity components between the seal and rotor are represented by x, y, $\dot{x}$, and $\dot{y}$ respectively. Direct terms develop reaction forces in the direction parallel to the input displacement or velocity. Cross-coupled coefficients define the reaction forces orthogonal to an input displacement or velocity vector. They arise due to fluid rotation.

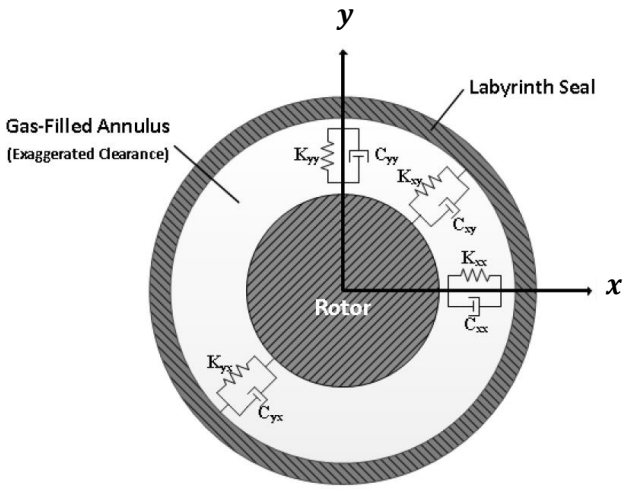

Figure 3. Dynamic model of a gas labyrinth seal with a centered rotor. Reprinted from [6].

For a centered position, Eq. (1) can be simplified assuming $K_{xx} = K_{yy} = K$, $K_{xy} = -K_{yx} = k$, $C_{xx} = C_{yy} = C$, and $C_{xy} = -C_{yx} = c$ to obtain

$$-\begin{Bmatrix} f_{seal_x} \\ f_{seal_y} \end{Bmatrix} = \begin{bmatrix} K & k \\ -k & K \end{bmatrix} \begin{Bmatrix} x \\ y \end{Bmatrix} + \begin{bmatrix} C & c \\ -c & C \end{bmatrix} \begin{Bmatrix} \dot{x} \\ \dot{y} \end{Bmatrix} \tag{2}$$

Figure 4 shows a rotor spinning at a frequency ω and precessing in the same direction at the frequency Ω about a radius e_0 from the center of the seal. Forward precession occurs when both the precession and spin are in the same direction, in this case counterclockwise.

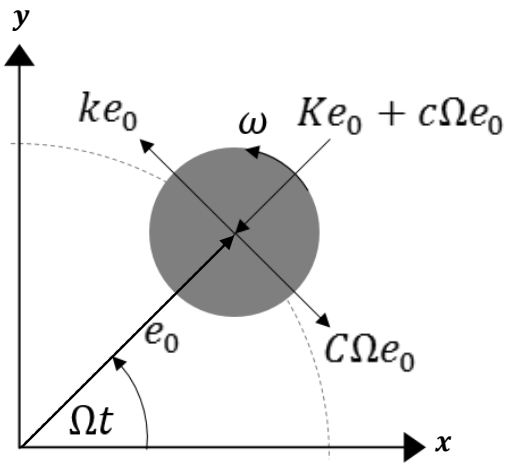

Figure 4. Direct and cross-coupled seal reaction forces acting on a forward precessing rotor.

Backward precession takes place when the rotor is precessing in the direction opposite to the spin. Rotordynamic coefficients act in the radial and circumferential directions. Positive direct stiffness *K* and cross-coupled damping *c* move the rotor radially towards the center of the seal. Direct damping acts like drag in the precession of the rotor; when positive, it drags the rotor back in the circumferential direction. Cross-coupled stiffness *k* is due to the fluid circumferential velocity. A positive *k* pushes the rotor circumferentially further in the direction of precession, making it a destabilizing force.

Figure 5 shows the forces resulting from backward precession. In case of backward precession, reaction forces due to damping terms *c* and *C* change direction because drag due to precession changes direction. The stiffness-related forces maintain the same direction.

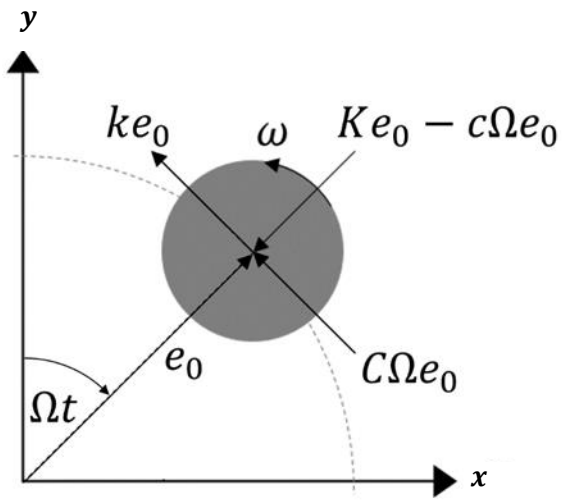

Figure 5. Direct and cross-coupled seal reaction forces acting on a backward precessing rotor.

The rotating components in turbomachinery introduce circumferential velocity, known as swirl, into the working fluid. Fluid rotation becomes important due to its effect on *k* and the system's stability. Swirl entering the seal is referred to as preswirl and is commonly characterized by the ratio of the inlet preswirl velocity, $V_{\theta 0}$, to rotor surface speed, $R\omega$, known as preswirl ratio (*PSR*). Positive *PSR* occurs with fluid rotation in the direction of rotor spin

$$PSR = \frac{V_{\theta 0}}{R\omega} \tag{3}$$

Swirl brakes can be installed upstream of seals to reduce *PSR*.

Effective damping relates both *C* and *k* to characterize the net damping force of the seal in the circumferential direction. A positive C_{eff} describes a seal with a net stabilizing effect.

$$C_{eff} = C - \frac{k}{\Omega} \tag{4}$$

The whirl frequency ratio (*WFR*) is another way of characterizing the stability of a seal in the circumferential direction. *WFR* is calculated as follows

$$WFR = \frac{k}{C\omega} \tag{5}$$

Similarly, effective stiffness accounts for both radial coefficients *K*, and *c* as

$$K_{eff} = K + c\Omega \tag{6}$$

In 1980, Benckert and Wachter [7] presented the first *K* and *k* measurements for interlocking labyrinth seals. Static loads were applied to vary the rotor's eccentricity, and the resulting pressure fields were measured and integrated. No dynamic excitation was applied, and thus no damping data was recorded. Swirl brakes are installed upstream of the seals to analyze the effects of *PSR*. Their tests showed negative values of *K* and positive values of *k* that increase proportionally with *PSR*, proving the use of swirl brakes to be effective in reducing PSR and cross-coupled stiffness *k*.

Using a hydraulic-shaker, Childs and Elrod [8] are the first to measure stiffness and damping coefficients of interlocking gas labyrinth seals. Measurements were obtained for different pressure ratios, excitation frequencies, and rotor speeds. Their results show frequency-dependent rotordynamic coefficients. They say that "[the] results are disturbing to the extent that they conflict with the generally-held view that rotordynamic coefficients provide a frequency-independent relation between reaction-forces and motion".

In 1999, Baumann [9] measures damping and natural frequency of a compressor using interlocking labyrinth seals with a discharge pressure of up to 400 bar; rotordynamic coefficients are not provided. A wide variety of seal and swirl brake configurations is tested using two different test rigs. All configurations using interlocking seals show a decrease in the natural frequency of the machine with increasing discharge pressure. See-through seals do not display this behavior. The configuration with the most interlocking seals depicts a 50% decrease in the natural frequency. Baumann theorizes that PSR and axial positioning could be possible causes of the distinctly negative radial forces of this seal.

Vague, scarce, and marginal data for interlocking seals motivated the development of a test rig to measure their rotordynamic coefficients. This work presents rotordynamic measurements of a see-through labyrinth seal using a test rig that can be used to test interlocking seals. Comparing the results to the considerable amount of literature on see-through seals serves to validate the test rig.

2. PROCEDURE

An adaptation of test methods by Millsaps et al. [10] and Wagner et al. [11] is used in this study. Both methods measure the dynamic pressure to calculate the forces inside a labyrinth seal and extract rotordynamic coefficients. Figure 6 shows the resulting circumferential and radial forces in a seal that is precessing with eccentricity, e_0. The pressure builds up and lags the position vector by an angle β. The pressure results in radial F_r and circumferential F_θ force components, that are used to calculate the seal's rotordynamic characteristics.

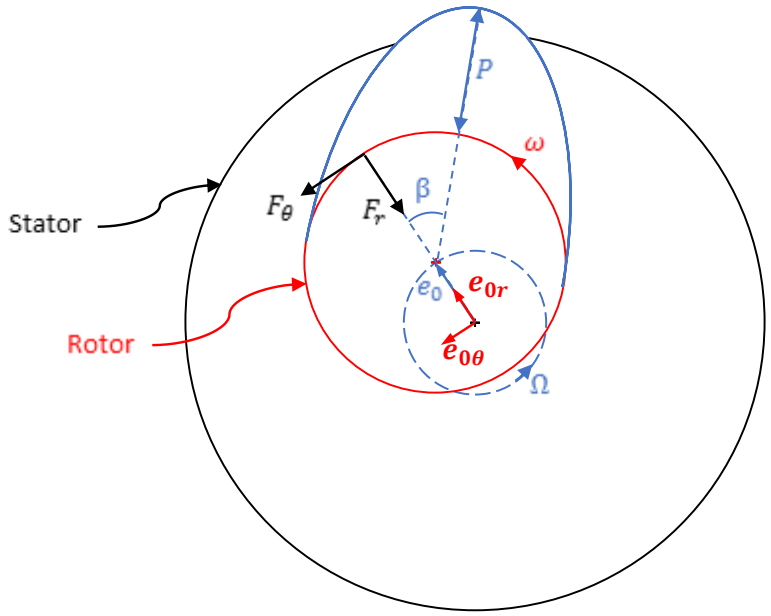

Figure 6. Schematic of reaction forces in the seal due to the rotor's displacement.

Millsaps et al. [10] test a single-cavity see-through TOR seal using a differential pressure transducer. They test at backward and forward precessions up to 40 Hz using a nested bearing arrangement. The circular precession of the rotor results in a dynamic pressure wave that is measured and integrated over the surface area to obtain the forces

applied by the air on to the rotor. These forces, plus position measurements obtained via proximity probes, allow for the calculation of the seal's dynamic coefficients.

Childs [12] rederived the equations used by Millsaps to decompose dynamic pressure into radial and circumferential forces in the seal (found in Appendix A). Rotordynamic coefficients are obtained from such equations. For forward precession, the radial and circumferential forces are

$$F_r = L_c R\pi P \cos\beta = e_0(K + c\Omega) \tag{7}$$

$$F_\theta = L_c R\pi P \sin\beta = e_0(k - C\Omega) \tag{8}$$

As shown in Fig. 7, Millsaps et al.'s results show circumferential forces that decrease linearly with increasing precession frequencies. Measurements for different spin rates fall on parallel lines, meaning similar damping values. The cross-coupled stiffness *k* is larger for spin rates going against the inlet swirl, in this case at -418 rad/s.

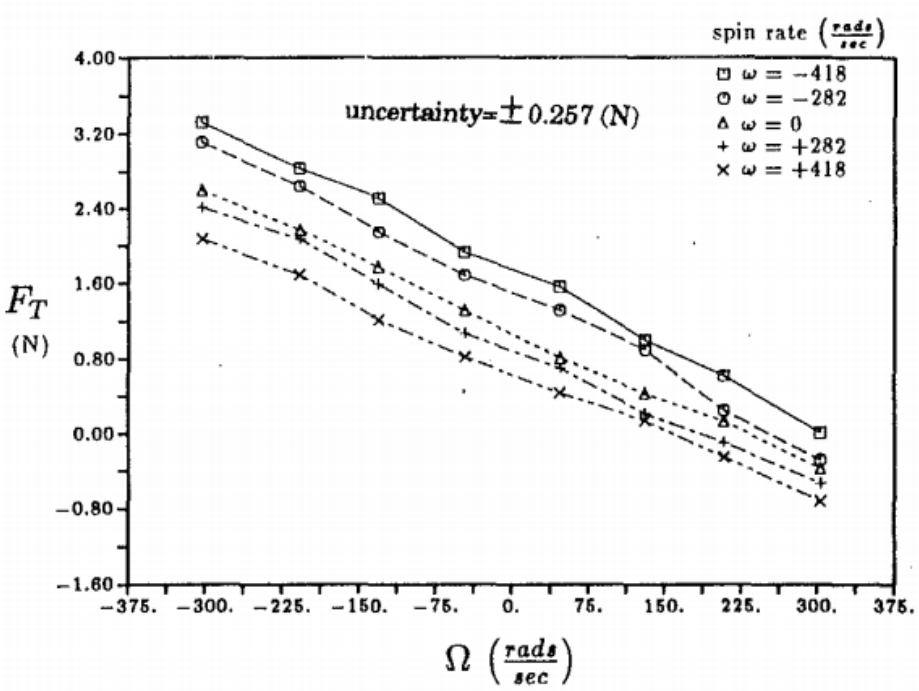

Figure 7. Measurements of circumferential force as a function of precession frequency for single gland TOR seals by Millsaps. Reprinted from [10].

Each cavity contributes to the total seal forces. The seal forces are the summation of the individual cavities formed by the interlocking labyrinth. (Measurements of only one cavity are provided in this study.) Equations (9-12) would be used to compute the total seal forces

$$\sum_{n=1}^{i} F_r^+ = \sum_{n=1}^{i} L_c\, R\pi P_i \cos\beta_i = e_0(K + c\Omega) \tag{9}$$

$$\sum_{n=1}^{i} F_\theta^+ = \sum_{n=1}^{i} L_c\, R\pi P_i \sin\beta_i = e_0(k - C\Omega) \tag{10}$$

$$\sum_{n=1}^{i} F_r^- = \sum_{n=1}^{i} L_c\, R\pi P_i \cos\beta_i = e_0(K - c\Omega) \tag{11}$$

$$\sum_{n=1}^{i} F_\theta^- = \sum_{n=1}^{i} L_c\, R\pi P_i \sin\beta_i = e_0(k + C\Omega) \tag{12}$$

where *i* is the number of cavities, and the superscripts +, and - indicate the direction of precession. Equations (9-12) are divided by e_0 to yield linear equations of rotordynamic coefficients where damping is the slope and stiffness the *y*-intercept of the line as shown in Fig. 8. Measurements of radial force at different frequencies would result in a line as depicted by Sketch (A). Sketch (B) represents a line of circumferential force measurements for a range of frequencies similar to Millsaps' measurements (see Fig. 7). All coefficients have positive values in the figure although this is not necessarily true for measured results; e.g., Arthur [5] presents negative direct stiffness for *TOS* seals. Millsaps et al.'s measurements for backward and forward frequencies formed a continuous lines. A linear regression method can be used to test the goodness of fit and accuracy of such lines. Coefficients are easily extracted from the linear regression equation using slope and intercept.

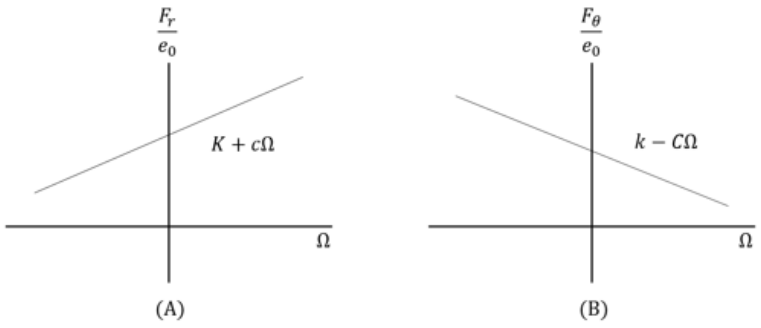

Figure 8. Predicted normalized radial (A) and circumferential (B) forces.

At least two different precession frequencies are required to solve for the rotordynamic coefficients. F_r/e_0 and F_θ/e_0 are plotted as a function of precession frequency Ω. Individual coefficients at a given frequency can be obtained by combining the forward and backward results in Eqs. (8-11) as follows

$$F_r^+ + F_r^- = -2Ke_0 \tag{13}$$

$$F_\theta^+ - F_\theta^- = -2Ce_0\Omega, \qquad \Omega > 0 \tag{14}$$

$$F_\theta^+ + F_\theta^- = 2ke_0 \tag{15}$$

$$F_r^+ - F_r^- = -2ce_0\Omega, \qquad \Omega > 0 \tag{16}$$

This study presents results for forward and backward excitation frequencies between -50 Hz and 50 Hz. Plots of forces and rotordynamic coefficients are provided as a function of frequency for a range of inlet pressures and pressure ratios. No swirl brakes are used although the test rig enables their use for future projects. All tests are performed at 0 and 10 kRPM. Each test configuration is tested eight separate times for repeatability analysis.

3. TEST APPARATUS

Wagner et al. [11] use magnetic bearings to precess a rotor-seal assembly at 15 kRPM and Ω values ranging between -400 Hz and 400 Hz. The rotordynamic characteristics of a see-through TOR labyrinth seal are obtained by two methods: dynamic pressure measurements, magnetic bearing calibration, and compared to CFD. The authors measure small forces with large uncertainties and state, "The results obtained from the dynamic pressure measurement provide the highest level of confidence for these short seals."

In 2006, Zutavern [13] presented his doctoral dissertation with focus on measuring rotordynamic forces in magnetic bearings using fiber optic strain gauges in a test rig at the Turbomachinery Lab. The facility seen in Fig. 9 has been modified to test interlocking labyrinth seals. Magnetic bearings (1) with a combined load capacity of 3.5 kN (800 lbf) support a rotor (2) weighing 900 N (200 lbf). Removing the inertia disks (3) used by Zutavern reduced the bearing span and weight of the rotor. The rotor's first critical speed occurs at 280 Hz. The PID controller and filter settings for the magnetic bearings were adjusted for the new rotor. Laminated sleeves (4) are needed to provide the magnetic forces, and catcher bearings (5) for rotor support in case of an alarm or a loss of power. A flexible Rexnord coupling (6) connects the emergency brake (7) to the rotor. A quill shaft (8) attaches to the V-belt pulley (9) that connects to the motor sitting behind the Test stand (10). The test section occupies the area denoted by the dashed lines (11).

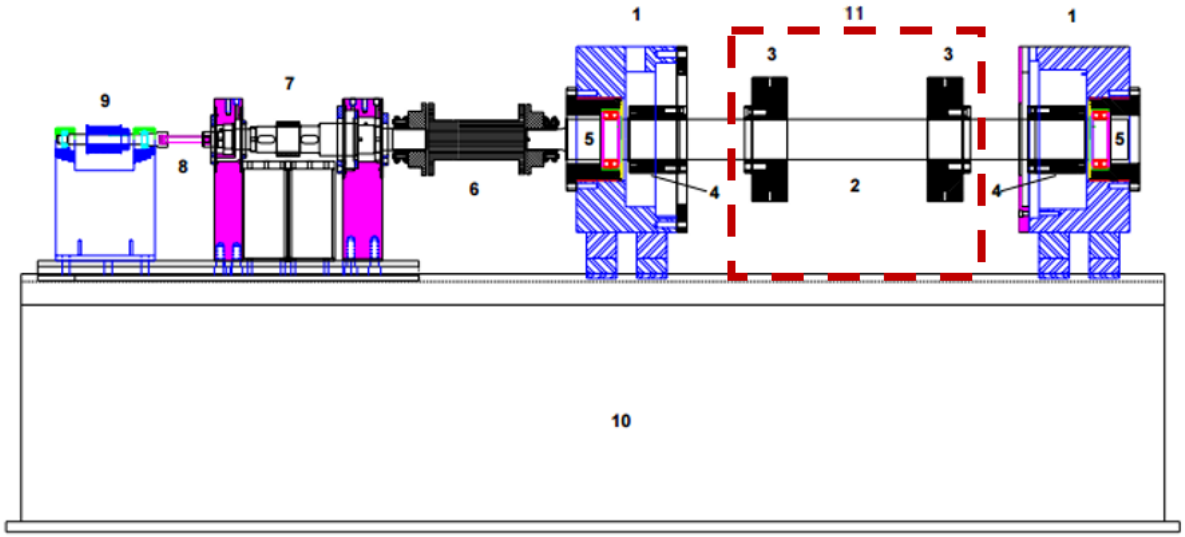

Figure 9. Test rig used by Zachary Zutavern for doctoral dissertation in 2006. Reprinted from [13].

Figure 10 shows a section view of the test stator. It is symmetric about the rotor's axis of rotation. All housing components are split along the horizontal plane to enable testing of interlocking labyrinth seals (shown in Fig. 11 and Fig. 22). Precise alignment of each individual semi-circular component was challenging and crucial (more in section 3.7). Two identical *TOS* seals located back-to-back minimize the thrust caused by the pressure drop across the seals. Pressurized air enters through the inlet ports (1) where the inlet temperature is measured. It flows through a swirl vane (2), discussed in the following section. The space (3) between the swirl vane and the seals is occupied by a swirl brake, or a smooth ring that is used in case of a no-swirl-brake test condition. Air enters the seal composed of *TOS* (4) and a smooth seal (5) shrunk onto the rotor (6). Exhaust chambers (7) and exit labyrinth seals (8) collect the air into exit hoses. Exhaust pressure and temperature is measured at the *NDE* exhaust chamber. Back pressure is regulated with a valve located downstream of a pipe that connects the exhaust hoses. Pressure ratios of 0.5, 0.6, 0.7, and 0.8 are tested.

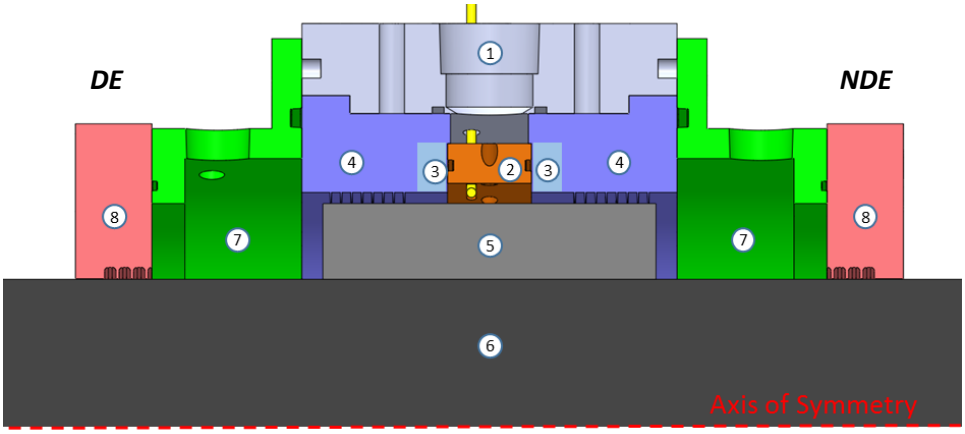

Figure 10. Components of test section.

Figure 11 (A) shows a fully assembled test rig. Precise alignment is crucial to obtain accurate measurements. Aligning the stator and rotor is the most challenging step in an assembly due to the number of concentric components. The process starts by centering the rotor within the magnetic bearings by bumping it against the catcher bearings to find the center location. Meanwhile, the stator components are assembled around an alignment mandrel (see section 3.7). The stator is opened by the bore's centerline forming two stator halves (top and bottom). The top and bottom halves are rejoined around the (levitated and centered) rotor and supported by pedestals. Shimming the pedestals to improve alignment is common. The rotor must spin freely before moving on to precision alignment (section 3.8).

Figure 11 (B) shows the top and bottom stator halves surrounding the rotor. Liquid sealant in the split faces reduces leakage along the split line dramatically. Leakage, alignment, and roundness of components are the most prevalent issues with the test rig. Meticulous alignment, the use of o-rings and sealants, and precision machined parts are necessary to obtain sensible data.

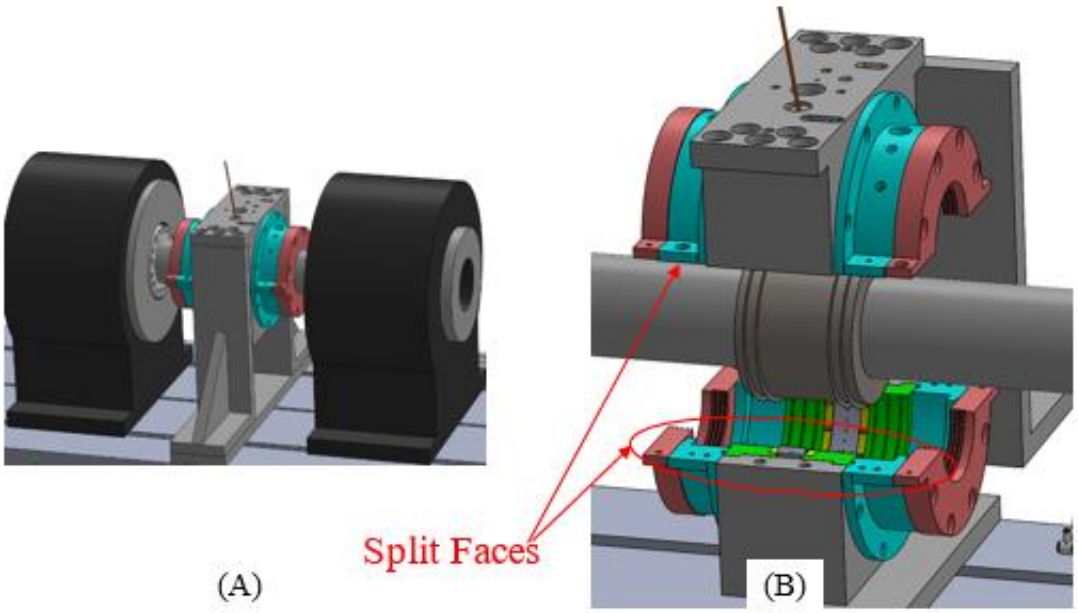

Figure 11. CAD model of (A) fully assembled test rig, and (B) an exploded view of the test rig showing the top and bottom stator halves. Reprinted from [14].

3.1 Swirl Vane

Swirl vanes direct the flow with a circumferential component into the test seals as shown in Fig. 12. This study implements a swirl vane design that yields a 0.5 *PSR*. O-ring grooves prevent leakage through the sides of the swirl vane. 16 holes on each side of the swirl web accelerate the air to the desired swirl velocity. Changing the geometry and number of holes changes the *PSR*. Swirl is measured with a Pitot-tube located upstream of the *NDE* seals as shown in Fig. 12. The Pitot tube is angled directly at the circumferential direction of the air at the entrance of the seal. The inlet static pressure is measured at this location.

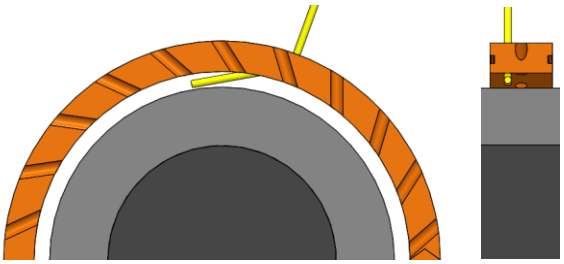

Figure 12. Swirl vane design with Pitot tube location.

The difference between the total and static pressures through the Pitot tube is the dynamic pressure. Simplifying an equation by Bernoulli, the circumferential velocity is determined by

$$V_{\theta_0} = \left[\frac{2(P_T - P_s)}{\rho}\right]^{1/2} \tag{15}$$

Finding the hole geometry that results in the desired swirl ratios is challenging. The correct geometries are found using mass conservation equations, simple CFD analysis, and an iterative trial and error testing of 3D printed swirl vanes.

3.2 Swirl Brakes

Swirl brakes obstruct the path of flow to reduce the circumferential velocity of the fluid. A swirl brake spacer follows the inlet swirl vane. A swirl brake or a smooth seal is installed in the spacer to test the rotordynamic performance with or without swirl brakes. Figure 13shows the spacer without (A) and with a swirl brake (B). The swirl brakes have the same radial clearance as the labyrinth teeth in the seals. A pressure tap downstream of the swirl brake spacer allows for measurements of pressure drop across the swirl brake. This study does not implement swirl brakes, and thus there is no pressure drop between the inlet swirl vane and the seal inlet.

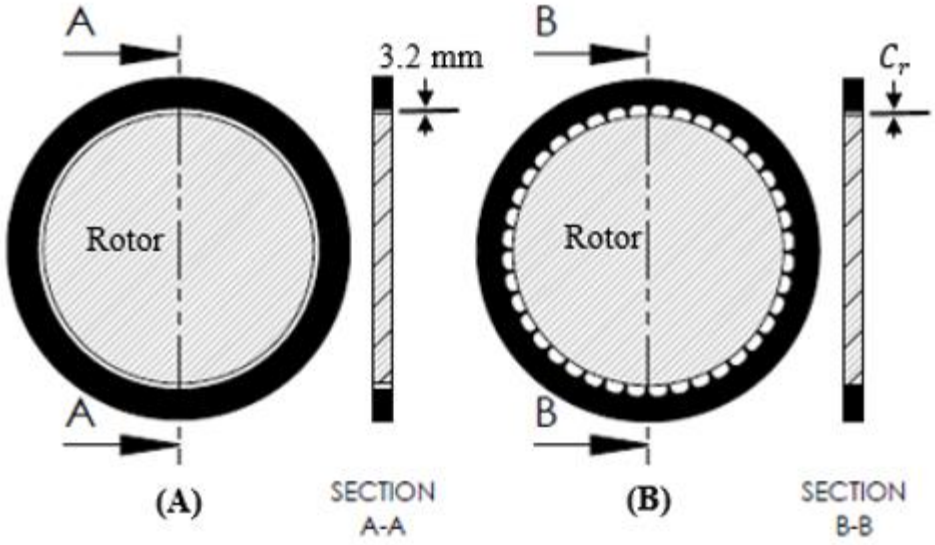

Figure 13. Front view of spacer ring (A) and swirl brake (B) possible options.

3.3 Test Seals

Figures 14 and 15 are the detailed seals' drawings. The *TOS* seal has eight teeth. The cavity length L_c, between labyrinth teeth, is 3.5 mm. Each tooth is 3.5 mm high and 0.25 mm thick at the tip. The radial clearance C_R, is 0.2 mm. The smooth seal rotor is shrunk onto the shaft.

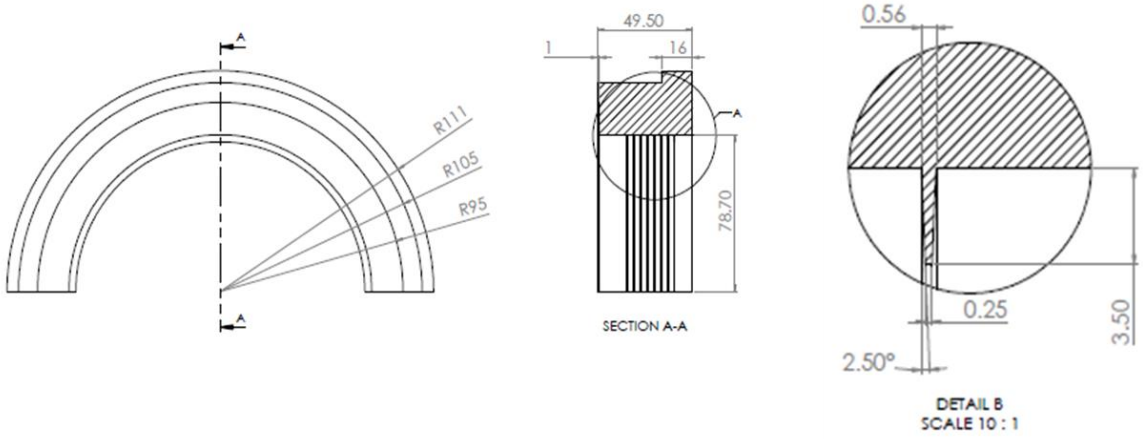

Figure 14. *TOS* seal drawings in mm.

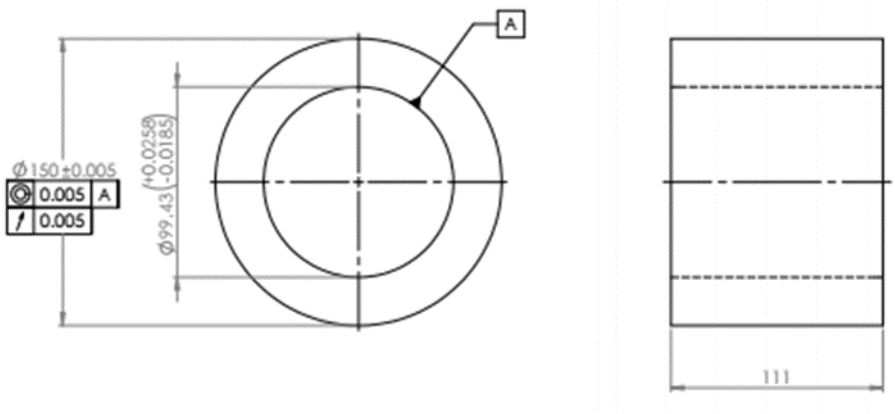

Figure 15. Smooth seal rotor shrunk onto shaft drawings with units of mm.

3.4 Instrumentation

After several years of struggle using flush-mounted piezo-electric pressure sensors to measure the pressure inside the seals' cavities without success, the test rig was modified to use Millsaps' technique of a differential-pressure transducer. This technique permits the measurement of small, time-varying oscillations on top of a large static pressure, as encountered here. Figure 16 shows the working mechanism of a differential pressure transducer that is unloaded (A), positively loaded (B) and negatively loaded (C). The total pressure, P_T, in the seal enters the high port of the transducer, while a static pressure, P_S, connects to the low port. This method captures small perturbations regardless of large static pressures due to the balancing pressures in the diaphragm. The output voltage is zero for equal pressures, positive when $P_T > P_S$, and negative when $P_T < P_S$. Supplying the correct P_S is required for precise pressure measurements.

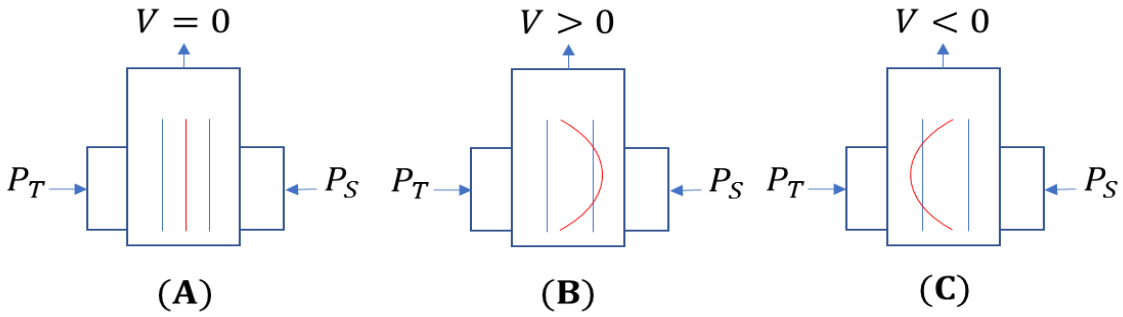

Figure 16. Schematic of diaphragm inside of differential pressure transducer with a balanced (A), positive (B), and negative (C) net pressure.

Two differential pressure transducers mounted 180° apart of each other in a cavity validate the existence of a precessing pressure wave when the peak pressure of one sensor is observed half a cycle after the other. Figure 17 shows the stator assembly with test seals, a swirl vane, two differential pressure transducers, and a damping plenum. The Top and Bottom differential pressure transducers measure the difference between P_S and P_T, which combines static and dynamic pressure due to the rotor's precession.

Both sensors are in the third cavity. 100 mm long stainless steel senselines connect the P_T port of the differential pressure transducers to the face of the seal. The author studied the effects of the pressure's phase and magnitude using different sense line lengths and materials. Long sense lines and soft materials lower the natural frequency and decrease the magnitude of the dynamic pressure signal. The effects of a 100 mm stainless steel sense line are negligible.

Two vibration-cancelling mechanisms combine to extract a precise P_S from the seals' cavity. The first method uses two 0.5 m long plastic tubes located 180 degrees apart from each other connecting the seal to the inlet of the damping plenum. Ideally these signals are out-of-phase with each other and cancel as they meet. The second method is a 305 mm long plenum filled with insulating fibrous material to dampen any dynamic excitation remaining in the line. P_S is developed at the damping plenum's exit and connects to the low port of the differential-pressure transducers.

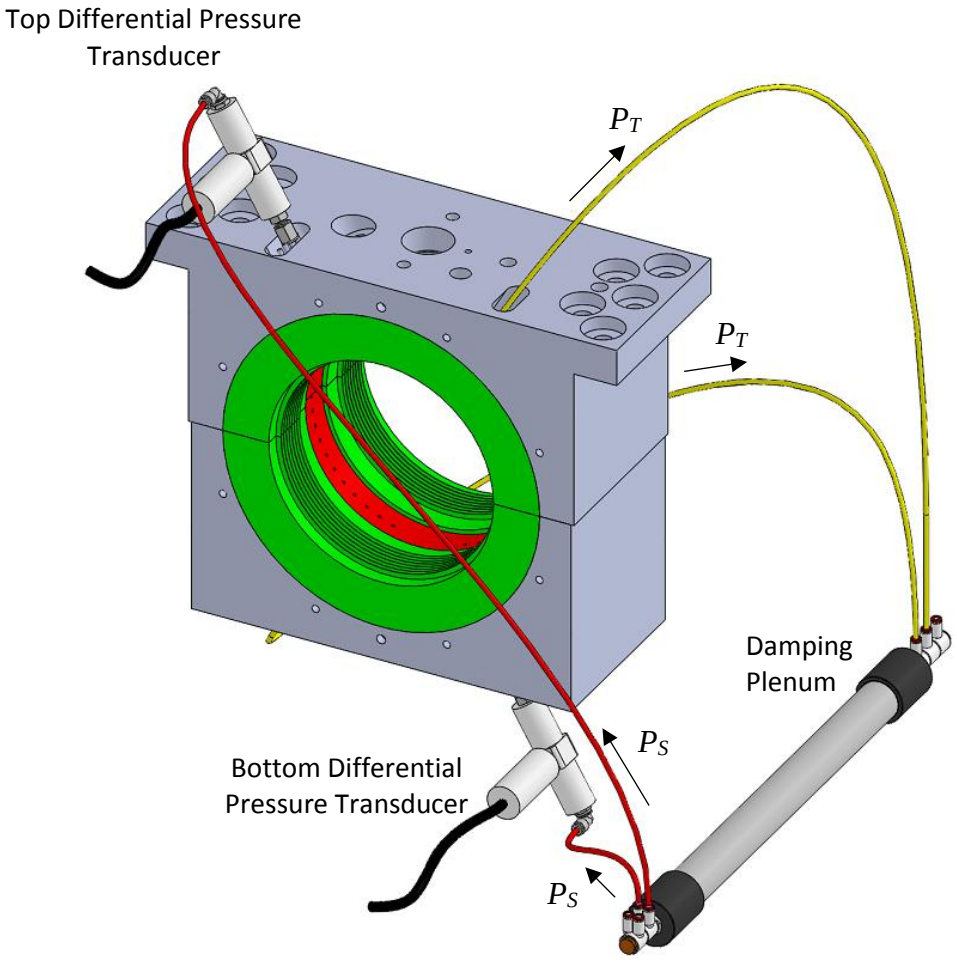

Figure 17. Differential pressure transducer and plenum installation in test section.

Experience shows the damping plenum is essential when implementing this technique successfully. The facility's final plenum design uses mineral fiber packed tightly into a piece of 305 mm long 25 mm diameter pipe. The plenum has extra inlet and outlet ports to measure inlet and outlet pressure. Tests show the effective reduction of 99.9% of the dynamic signal coming into the plenum.

Figure 18 shows a cross section schematic of the tested *TOS* seal. Seven cavities are formed from the eight teeth in the test seal. Millsaps tested a single cavity TOR see-through seal. This study presents data for only the third cavity. Upon validation, future

tests will require pressure sensors in all the seals' cavities. Each sensor has a resolution of 69 Pa, and a rise time of less than 2 microseconds.

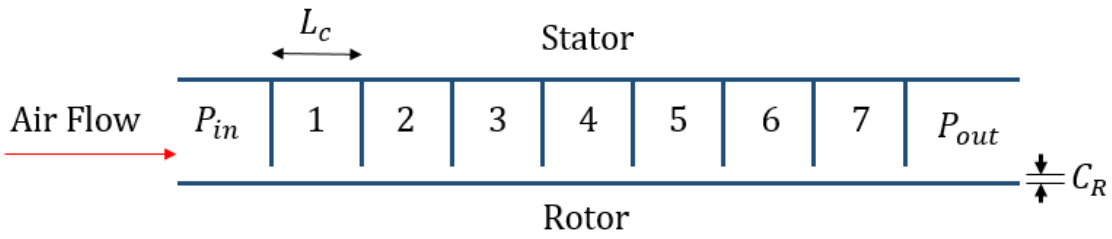

Figure 18. Schematic of labyrinth seal cross section.

Two pairs of orthogonal proximity probes located at the *DE* and *NDE* exhaust chambers measure the position of the rotor (see Fig. 10). Four Bently Nevada 3300 XL NSv proximitor sensors measure relative displacement on the *XDE*, *XNDE*, *YDE*, and *YNDE* axes. Each proximity probe has a resolution of 2.5 μm (0.1 mil) at room temperature for a range of 2.5 mm (100 mil). Figure 19 shows the placement of the position and pressure sensors along the circumferential direction of the rotor. Position probes are located in both the *DE* and *NDE* exhaust chambers. P_S signals from both differential pressure sensors are identical; they originate from the noise-filtering damping plenum upstream. Differential pressure transducers subtract P_S from P_T to give dynamic pressure P_d. For a centered circular precession orbit, the dynamic pressure in the Top and Bottom P_T signals should be identical except for a 180° phase lag due to their position relative to the rotor's precession. The angle β used in Eqs. 6-11 is measured individually for the Top and Bottom sensors using the differential pressure measurements and relative position to the rotor. All measurements are clocked to the *y* axis as reference (Ref.) for phase β calculations.

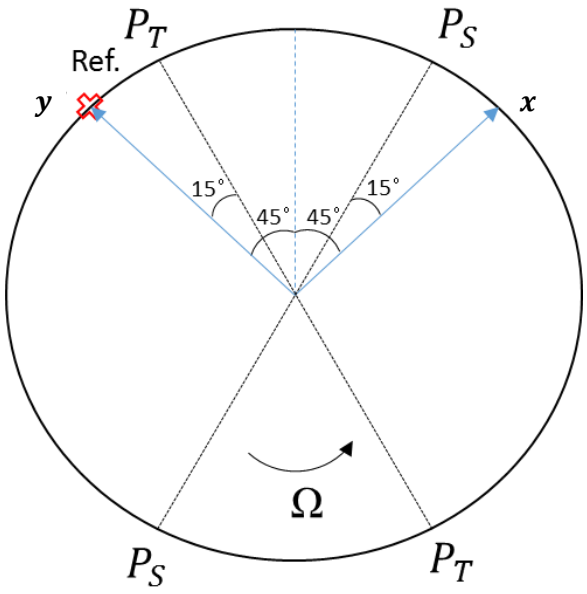

Figure 19. Pressure and position probe placement seen from the front of the *NDE* bearing.

Table 1 provides detailed information of the sensors used. Five proximitor sensors are used, four to measure the radial position of the rotor, and one serves as a tachometer. Pressure measurements are described in previous sections. Section 3.6 describes flow measurements. Calibration, at the lab or by the manufacturer, was performed the same year the tests were performed.

Table 1. Sensors used during tests.

Measurement	Number of Sensors	Brand	Model	Range	Error
Position	5	Bently Nevada	3300 XL NSv	2.54 mm	± 2.54 µm
Differential Pressure	2	Omega	MMDDB005 BIV5P4B0T1	0.34 bar	± 0.0007 bar
Static Pressure	2	Omega	PX329-300	20.7 bar	± 0.25 %
Flowmeter	1	Flow Technology	FT20NEE1 -GEH-5	0.25 to 2.86 m^3/min	± 0.25 %
Swirl Pressure	1	Emerson	3051CD4M22 A1AM5B4DF Q4	20.7 bar	± 0.0008 bar
Temperature	2	Omega	GG2036	-270 – 1372 °C	± 2.2 °C

3.5 Pressure Drop

Front and section views of the exit labyrinth seals are shown in Fig 20. Exit labyrinth seals and a back-pressure valve regulate the pressure drop across the seals. Exit labyrinth seals, located downstream of the exhaust chambers, have a 0.18 mm (7 mil) radial clearance with the rotor. The clearance is 0.02 mm (1 mil) tighter than the interlocking seals because they are easier to replace in case of contact with the rotor. The combination of *TOS* teeth and a ~10 mm land reduces leakage and supports the rotor during bump tests (described in section 3.8).

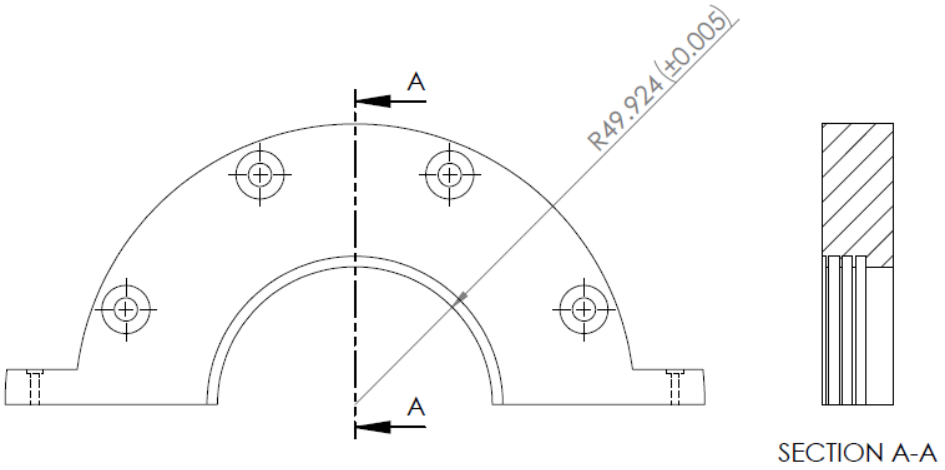

Figure 20. Front and side view of exit labyrinth seal with three teeth and a ~10 mm land for rotor support in case of contact.

Air collected in the exhaust chambers flows through hoses into a pipe with a control valve as shown in Fig 21. The hoses are located 180° apart from each other to minimize side loads. Fully closing the exhaust valve forces all of the flow to leak through the exit labyrinths, resulting in the minimum pressure drop possible across the test seals. Ambient pressure exit conditions are achieved with a fully open valve. Regulating this valve yields the desired pressure ratios of 0.5, 0.6, 0.7 and 0.8 at inlet pressures of 2.76, 3.79, and 4.83 bar. The test rig has a maximum available supply pressure of 20.7 bar inlet.

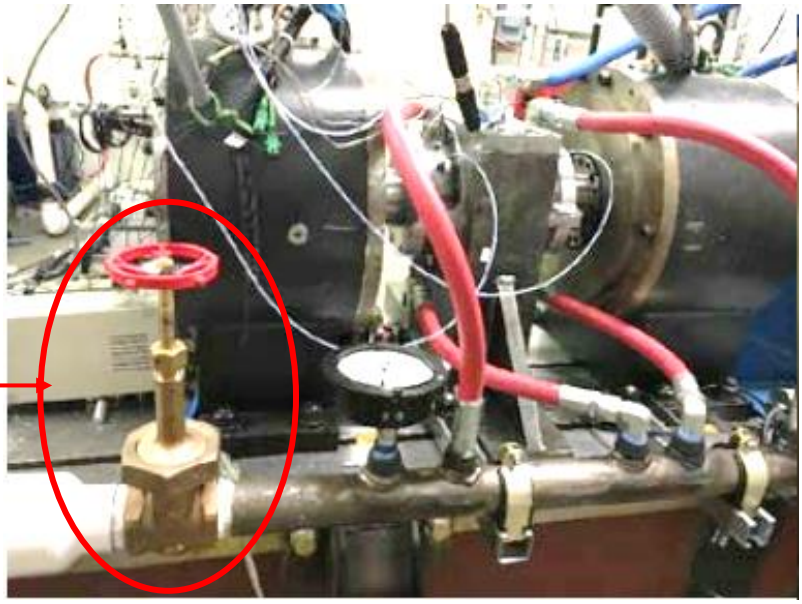

Figure 21. Back pressure control valve and exhaust hoses.

3.6 Leakage

Pressurized air passes through an FT-20 FTI turbine flowmeter with a 0.3% accuracy that measures the volumetric flow rate $\dot{Q}$ in Actual Cubic Feet per Minute (ACFM). Assuming negligible variations between the flowmeter and seal inlet the density ρ in kg/m^3 of air is

$$\rho = \frac{P}{287.06 * T} \tag{16}$$

where P is the pressure in Pa and T the temperature in K. Assuming zero leakage between the flowmeter and test section, the mass flow rate through each seal in kg/s is

$$\dot{m} = \frac{\dot{Q}\rho}{2119 * 2} \tag{17}$$

3.7 Alignment

A split housing is necessary to accommodate future testing of interlocking seals. A mandrel with tolerances tighter than the rotor's is used to align all the components in

the test section as shown in Fig. 22. The top and bottom parts of the stator are assembled around the mandrel. Bolts installed in holes (1) are tightened down to a torque of 8.5 N-m (75 in-lb) to join the seal halves. Four bolts (2) torqued down in small increments to 15 N-m (130 in-lb) join one half of the exit labyrinth to a half exhaust chamber. The exhaust chambers and exit labyrinths are joined similarly. Tightening all bolts in a star pattern allows for proper alignment. An aligned assembly allows for free movement of the mandrel. The top and bottom parts are disengaged to remove the mandrel. Alignment pins along the split line allow for the precise placement of the top and bottom on to the test TOS seals.

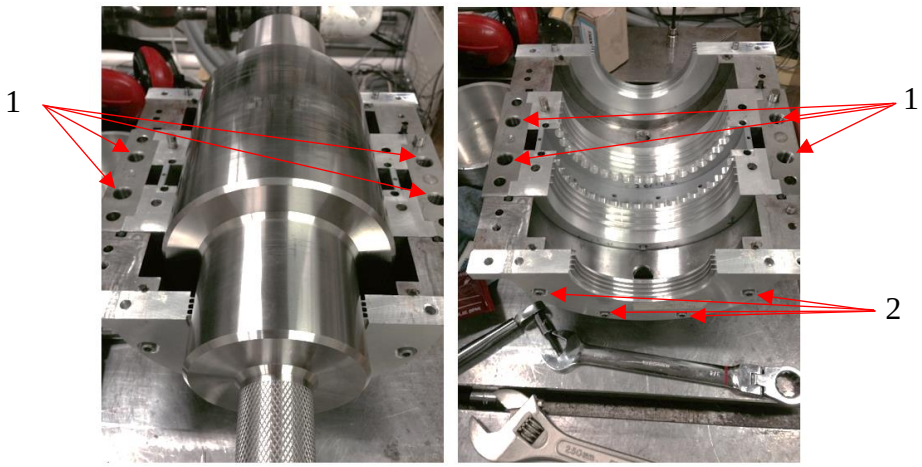

Figure 22. Mandrel used to align all parts of the top and bottom stator.

The four bolts used to join the stator for alignment are used to hold the stator around the levitating rotor as seen on Fig. 23. The stator is supported by a pedestal on each side that can be moved to adjust the alignment of the stator until the rotor is free to spin by hand. The pedestals are bolted down with 135 N-m (100 ft-lb) using a torque wrench.

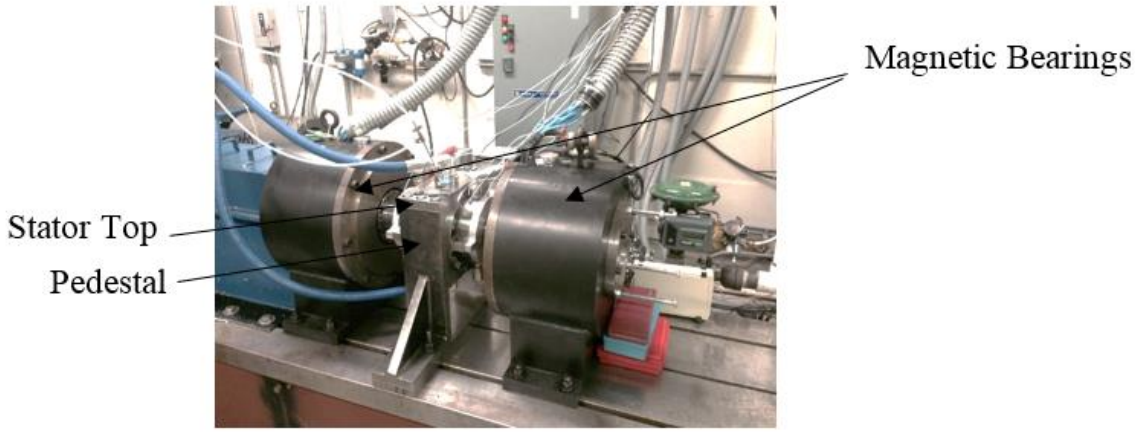

Figure 23. Stator full assembly.

The author's co-worker, Keith Gary, made great improvements to the alignment of the test rig, mainly by discovering that the stator's bore was out of round. Measurements improved dramatically after the stator was rebored. Alignment of components and the rotor have a large impact on the results.

3.8 Magnetic Bearings

Bearing calibration aligns the rotor with respect to the stator to prevent rubbing and obtain quality measurements. Centering the rotor within the stator consists of moving the rotor gently until contact is made and locating the rotor in a position equidistant from bump locations. Contact is usually made with the exit labyrinth seals because they have the smallest clearances (as shown in section **3.5**). MBScope's Calibration tool facilitates this procedure. Figure 24 shows a graph of electrical current vs rotor position during a bump test along the *y* axis. The rotor's position is proportional to the current until contact is made. The figure shows a radial clearance of 0.15 mm (6 mil), which is consistent with the design clearance between the exit labyrinths and the rotor. This procedure is followed for the *x* and *y* axes.

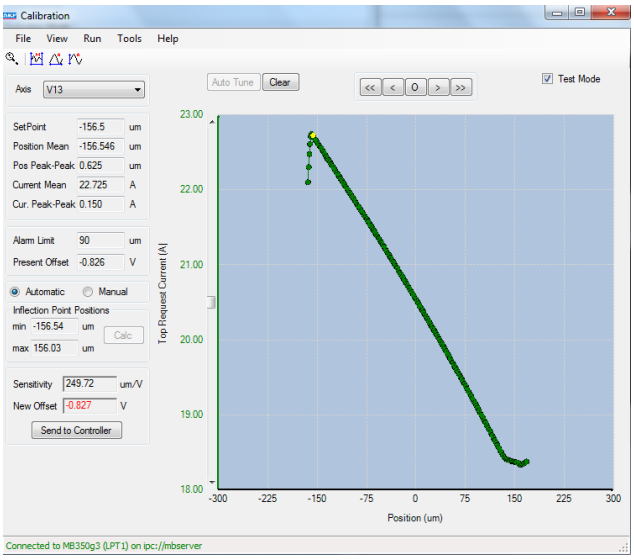

Figure 24. Bump test calibration of YDE axis, 0.15 mm radial clearance.

Clearance circles are obtained by recording the locations of the bump tests and tracing the largest possible circle within the points. Clearance circles are used to center the rotor and monitor the rotor's position relative to the seals during tests.

A logic system is programmed for safety. The logic prevents the motor from starting if the rotor is not levitated, or if oil is not being supplied to the ball bearings supporting the brakes' shaft. The logic system shuts off the motor, applies the brakes, and de-levitates the rotor if displacement or vibration exceed a safety limit.

3.9 Uncertainty

The Kline McClintock equation is used to calculate the propagation of uncertainty that the measurements have on the calculated quantities. The equation calculates the propagation of uncertainty of R as

$$w_R = \left[\left(\frac{\partial R}{\partial x_1} w_1\right)^2 + \left(\frac{\partial R}{\partial x_2} w_2\right)^2 + \cdots + \left(\frac{\partial R}{\partial x_n} w_n\right)^2\right]^{1/2} \tag{18}$$

Where R is a function of measured quantities $x_1, x_2, \ldots, x_n$, and w is the uncertainty. For example, the uncertainty of ρ composed of P and T is

$$w_\rho = \left[\left(\frac{w_P}{287 * T}\right)^2 + \left(\frac{-P * w_T}{287 * T^2}\right)^2\right]^{1/2} \quad (19)$$

Uncertainties are included in tables with the ± symbol, and with error bars in all graphs.

3.10 DAQ

The data acquisition system consists of six modules connected to an NI cDAQ-9178 chassis. The differential-pressure sensors and proximity probes are connected to three NI 9239 modules. These modules allow four ± 10 V inputs and have a 24 bit resolution at 50 kHz sampling frequency. A module with this capability is required to capture with detail the pressure wave generated inside of the seal at high frequencies. The thermocouples connect to an NI 9211, specifically made to amplify the small voltages output by thermocouples. Other sensors are read by an NI 9220 card with 16 channels. Finally, an NI 9263 module is used to output signals from the computer into the magnetic bearings. These signals are injected onto the four axes in the bearings (*XDE, XNDE, YDE,* and *YNDE*) to create the precession orbits needed. In Fig. 25, two oscilloscopes show the precession circles generated digitally and output via the NI 9236 module.

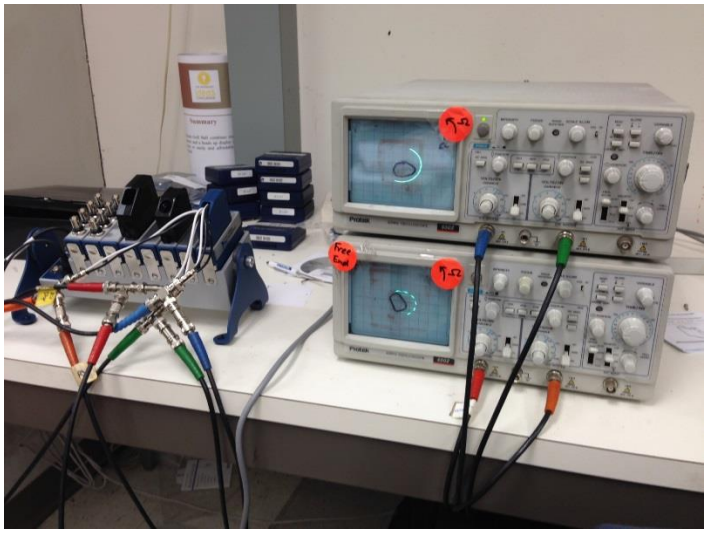

Figure 25. Injecting precession signals using module NI 9263.

3.11 LabView

LabView code is used to input and output signals. Two LabView VIs (Virtual Instruments) perform all signal processing. The Input VI displays all of the measurements and records data; the Excitation VI outputs the signals that precess the rotor. Figure 26 shows the Excitation and Input VIs working side by side. The Excitation VI on the left allows the user to select the precession frequency, in this case 40 Hz. The graph labeled Output shows the signals injected onto the four axes of the bearings. The Input VI on the right shows the actual measurements being recorded by the proximity sensors. The *DE* and *NDE* measurements show the path of the rotor as it precesses inside the clearance circles. To the right, data processed using live FFTs show the magnitude and frequency of the position. Peaks at 40 Hz verify that the excitation is at the desired frequency; the magnitudes equal the radii of the precession orbits.

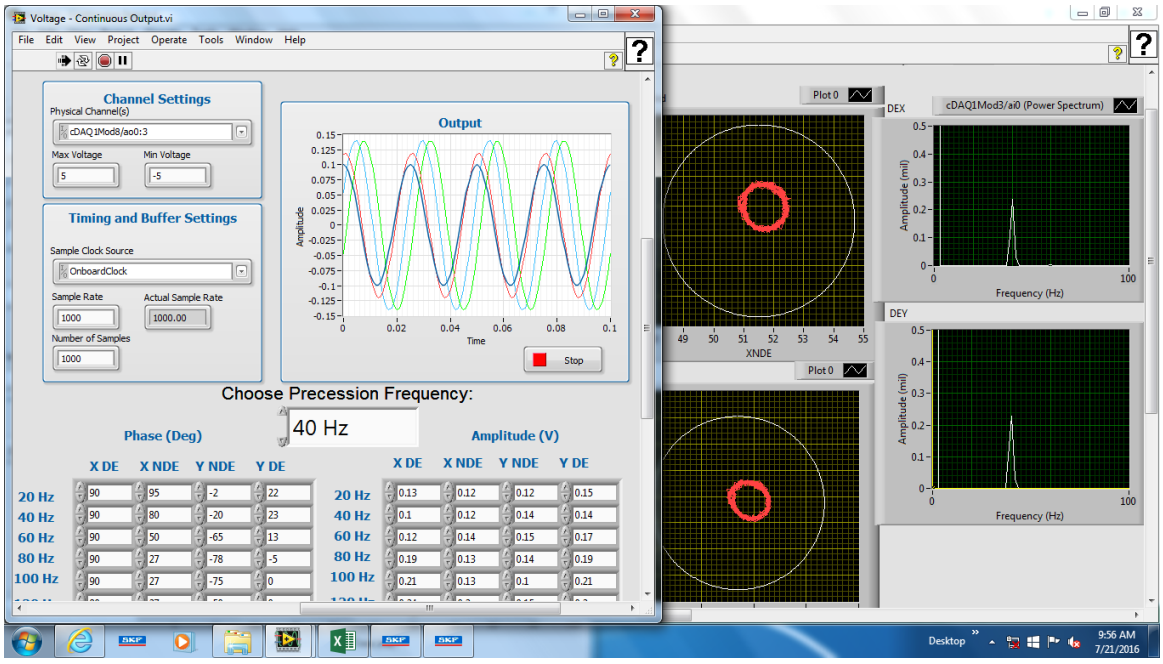

Figure 26. Excitation VI (left) used to precess the rotor at 40 Hz as seen in the Input VI (right).

The roundness of the orbits is evaluated using the phase difference between the position axes. Figures 27 and 28 show the phase of each proximity sensor referenced to that of *XDE* for forward and backward precession frequencies. A round precession circle requires an in-phase *DE* and *NDE* axes, and a 90° phase lag between *X* and *Y* axes. All tests are performed with precession circles that are within 10° of the desired phase value, whether it is 0° (in-phase) or 90°, marked by horizontal lines in each figure.

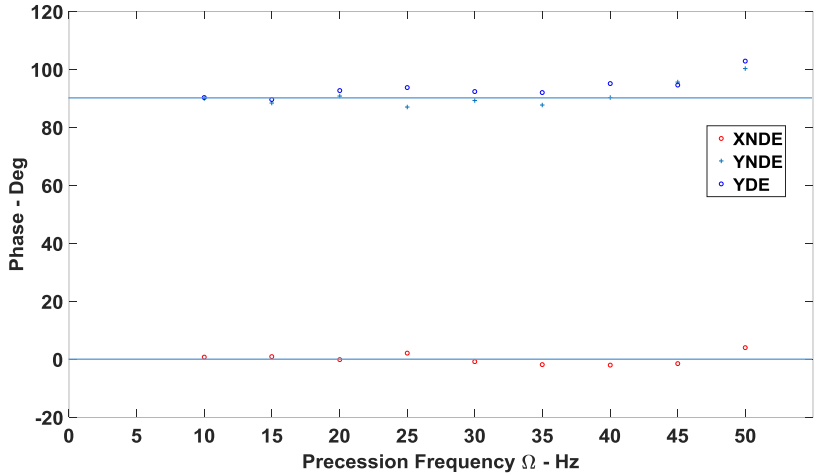

Figure 27. Roundness of forward precession orbit measured using the *XDE* phase as reference.

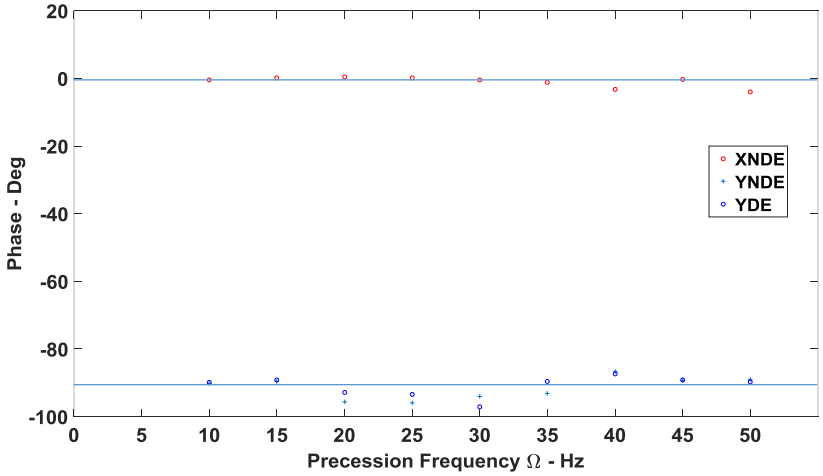

Figure 28. Roundness of backward precession orbit measured using the *XDE* phase as reference.

The Input VI is programmed to collect 40 thousand samples at 25 kHz, taking 1.6 seconds per test. Data are collected for steady state conditions at each precession frequency.

Figure 29 shows typical testing conditions analyzed with MBScope and LabView. The *DE* and *NDE* clearance circles and precession orbits are shown in the two

graphs to the right. The operator uses this VI to know useful information such as inlet pressure, swirl, flowrate, pressure drop, and rotor speed. The top left graph verifies that the *X* axis lags the *Y* axis by 90° in a circle with a radius of 33 microns.

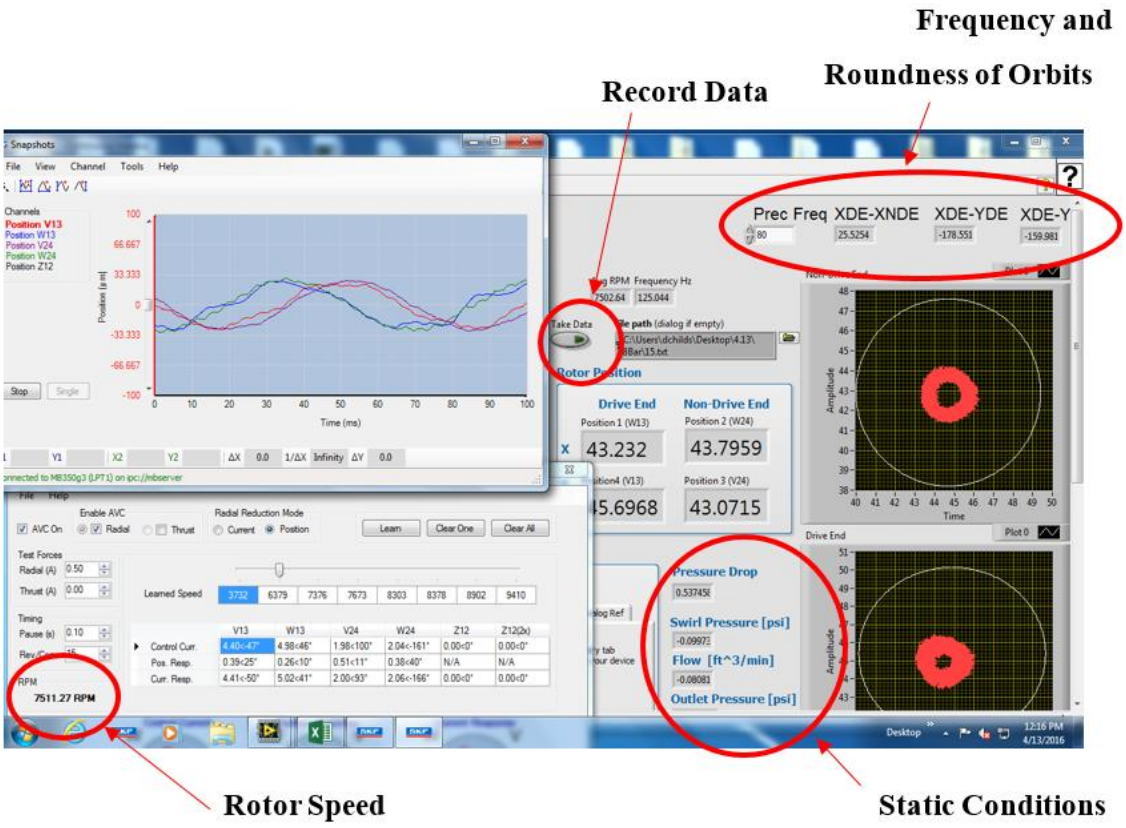

Figure 29. Monitoring tools and Input VI used while testing at 7.5 kRPM.

3.12 Repeatability

40 thousand samples of data are recorded in 1.6 seconds for each precession frequency. At 40 Hz the rotor precesses 64 times inside the seal while 625 samples of data are recorded per precession. Slicing the data in eight groups of 5,000 samples allows for repeatability analysis. This is done for all precession frequencies including 15 Hz, for which each group of data covers 3 precessions and more than ten thousand

measurements per precession. Determining error bars in the results is the motivation behind repeatability analysis.

3.13 Test Matrix

The proposed tests are performed with a rotor speed of 10 kRPM (167 Hz) and inlet pressures of 2.76, 3.79, and 4.83 bar. Tests at 0.5, 0.6, 0.7, and 0.8 pressure ratios are performed. The rotor is excited forwards and backwards at frequencies ranging from 15 to 50 Hz. The seal test matrix in Table 2 includes configurations at 0 and 10 kRPM, with three inlet pressures, four different pressure ratios, and eight forward and backward frequencies.

Table 2. *TOS* labyrinth seal testing conditions.

Rotor Speed kRPM	Inlet Pressure bar	Pressure Ratio	Forward Precession (Hz)	Backward Precession (Hz)
0	2.76	0.5	15, 20, 30, 35, 40, 45, 50, 55	15, 20, 30, 35, 40, 45, 50, 55
		0.6		
		0.7		
		0.8		
	3.79	0.5		
		0.6		
		0.7		
		0.8		
	4.82	0.5		
		0.6		
		0.7		
		0.8		
10	2.76	0.5		
		0.6		
		0.7		
		0.8		
	3.79	0.5		
		0.6		
		0.7		
		0.8		
	4.82	0.5		
		0.6		
		0.7		
		0.8		

4. DISCUSSION OF RESULTS

Results are presented in three different sections. Static results are shown first, followed by dynamic results of radial and circumferential forces as functions of frequency to extract rotordynamic coefficients. Finally, backward and forward precession frequencies are combined to show rotordynamic coefficients as functions of frequency. Straight lines connect the test points for visualization purposes.

4.1 Static Results

Table 3 shows the average static inlet and exit pressure for each test. The data of each test are sliced into eight groups of 5,000 samples. The error is calculated as one standard deviation between the average of all 40,000 samples and the averages obtained for each of the eight groups of 5,000 samples. The rotor speed error is 1 RPM or less for all cases. Temperature measurements show room temperature conditions with negligible variations from inlet to outlet. Pressurized air enters the test seal at 2.76, 3.79, and 4.83 bar. Small changes in inlet pressure within the same test configurations are due to the loss of air pressure in the accumulator downstream of the compressor. Regulating the exhaust valve yields the desired 0.5, 0.6, 0.7, and 0.8 pressure ratios. The pressure ratio is achieved within a 1% margin for all tests.

Table 3. Static pressure measurements for tests at 10 kRPM.

Inlet Pressure bar	Pressure Ratio	Inlet Pressure bar	Outlet Pressure bar	Pressure Ratio
2.76	0.5	2.41 ± .1	1.23 ± .04	0.510
	0.6	2.74 ± .04	1.68 ± .03	0.610
	0.7	2.90 ± .1	2.03 ± .06	0.700
	0.8	2.88 ± .06	2.30 ± .04	0.800
3.79	0.5	3.76 ± .1	1.94 ± .07	0.520
	0.6	4.09 ± .12	2.46 ± .07	0.600
	0.7	3.97 ± .06	2.80 ± .03	0.705
	0.8	3.76 ± .1	3.06 ± .06	0.814
4.83	0.5	4.81 ± .07	2.47 ± .04	0.513
	0.6	4.82 ± .08	2.96 ± .06	0.613
	0.7	4.49 ± .01	3.17 ± .01	0.706
	0.8	4.63 ± 0.07	3.67 ± .04	0.794

Figure 30 shows the measured *PSR* for all test configurations normalized to a rotor speed of 10 kRPM. That means, *PSR* for tests at 0 RPM is obtained dividing swirl velocity by the rotor surface speed at 10 kRPM. The obtained swirl ratios are close to the

desired 0.5 *PSR* and vary due to changes in pressure ratio and rotor speed. Designing the swirl vane that yields the desired *PSR* consists of an iterative process of CFD modeling and 3D printing. As expected, *PSR* decreases with decreasing inlet pressure and pressure differential. The effects of rotor speed are negligible.

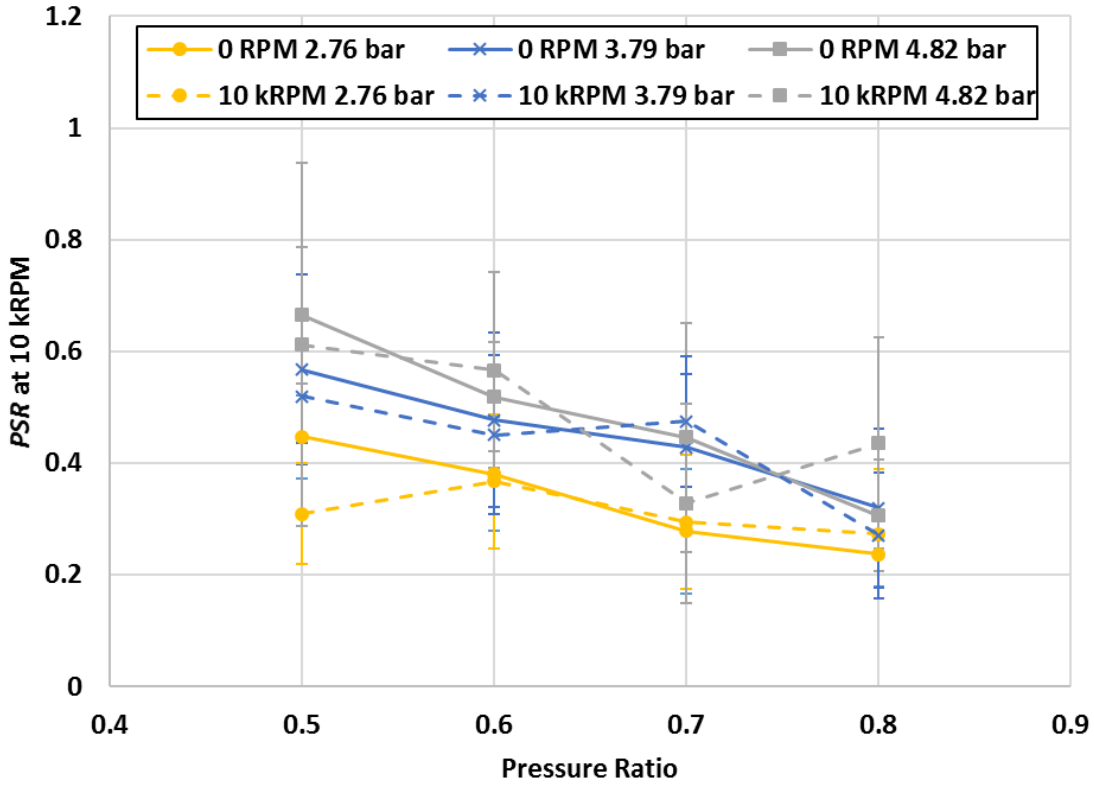

Figure 30. *PSR* measurements for range of inlet pressures tested at 0 and 10 kRPM.

Figure 31 shows $\dot{m}$ as a function of pressure ratio for all configurations. Flow rate increases with increasing inlet pressure and appears to be unaffected by either rotor speed or pressure ratio at low inlet pressures. The large difference in mass flow rate between tests at 0 and 10 kRPM at large inlet pressures suggest the influence of rotor speed on the mass flow rate is larger at higher pressures. Mass flow rate predictions using XLTRC^2 dismiss changes in flow rate due to rotor speed.

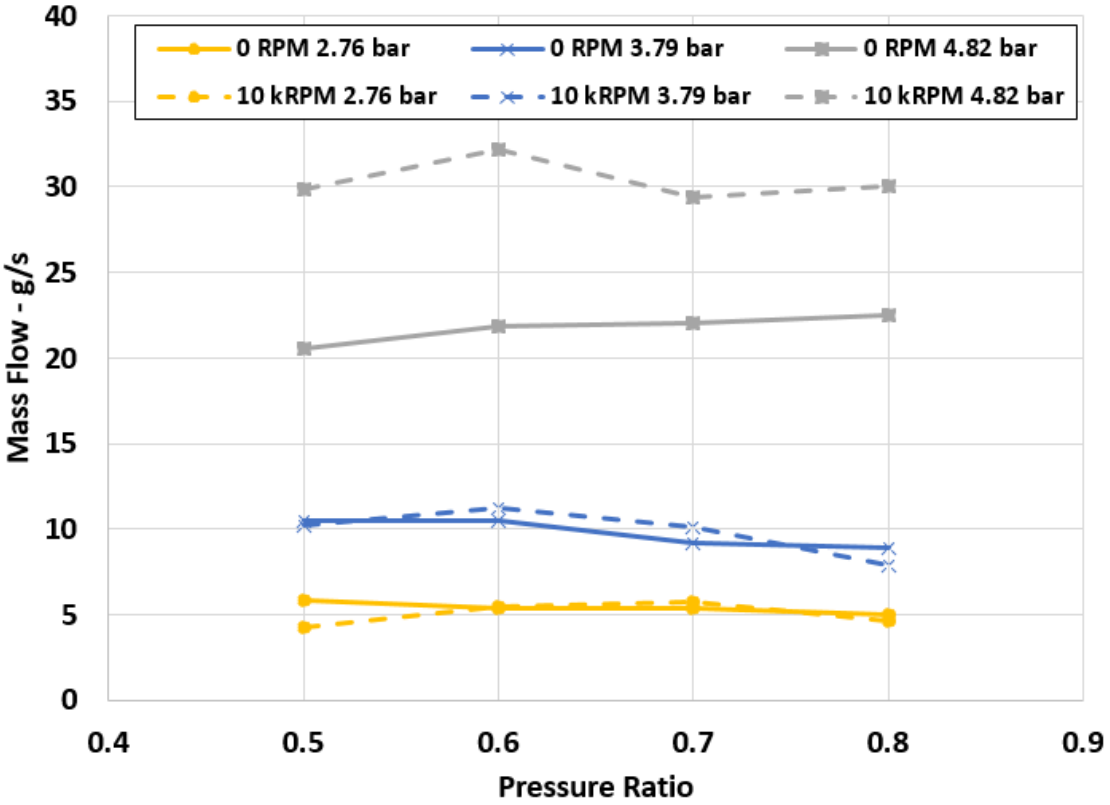

Figure 31. Mass flow rate vs Pressure Ratio.

Figure 32 shows predicted and measured values of mass flow rate for tests at 10 kRPM, different inlet pressures and pressure ratios. Predictions using XLTRC^2 with same test conditions and seal geometry overestimate the mass flow rate measured. Tests at high inlet pressure and pressure ratio agree the most with their predicted values. XLTRC^2 effectively captures the curvature in the lines due to inexact values of inlet pressure and pressure ratio (i.e. PR = 0.61 instead of 0.60).

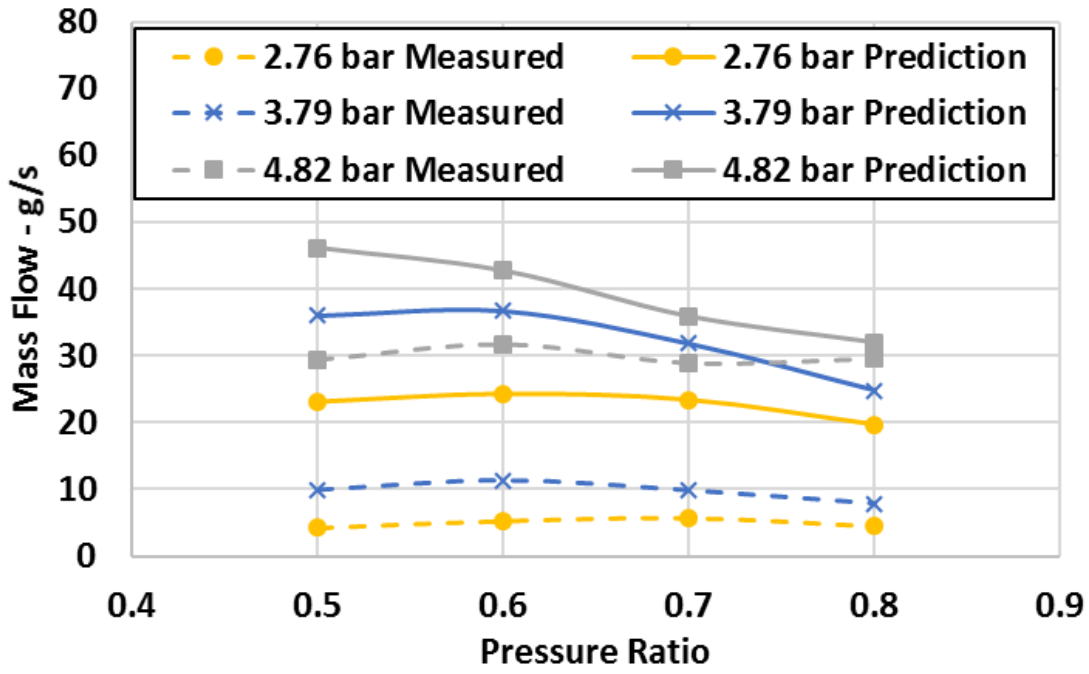

Figure 32. Measured and predicted mass flow rate vs Pressure Ratio at 10 kRPM.

4.2 Dynamic Forces

Dynamic data are obtained by precessing the rotor inside the seal for different frequencies. Figure 33 shows the radii of eccentricity e_0 used during tests. The precession orbits are between 20% and 30% of the radial clearance. Larger eccentricities proved to be difficult for the bearings to control. Forward and backward tests have similar eccentricities. Frequencies larger than 80 Hz are difficult to excite with eccentricities larger than 10% of the clearance. The eccentricity e_0 is used to calculate the rotordynamic force coefficients.

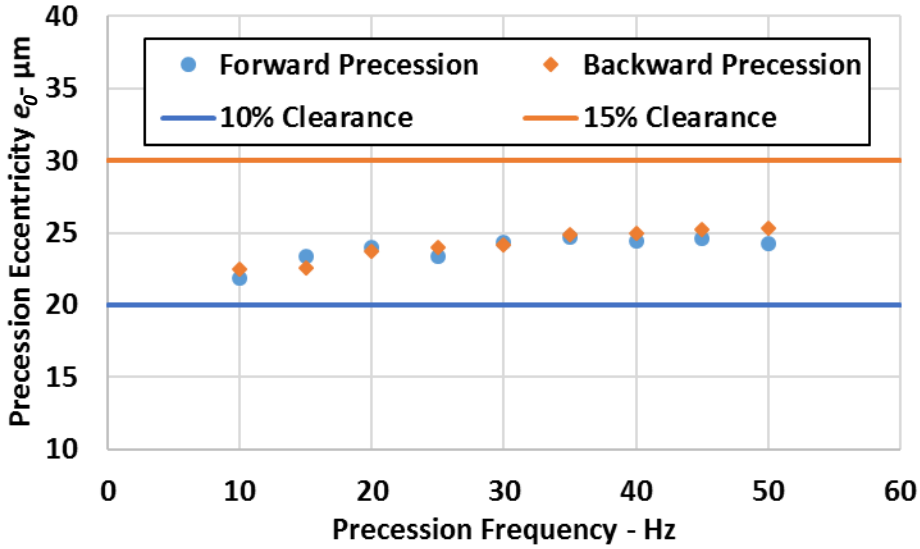

Figure 33. Radius of precession eccentricity e_0.

Figure 34 shows typical time response measurements of position and pressure versus an ideal 50 Hz sine wave. The graph shows the *YDE* position and the dynamic pressure in the bottom and top differential pressure transducers. This example is for a rotor precessing at 50 Hz, for a 3.79 bar inlet pressure with a 0.5 *PSR*. The Top and Bottom differential pressure transducers show a 180° phase shift that confirms the passing of a pressure wave as the rotor precesses. Although the trend is clear, obtaining the exact magnitudes of P and e_0, and the phase β between the two signals is difficult in the time domain; Fourier analysis facilitates this test.

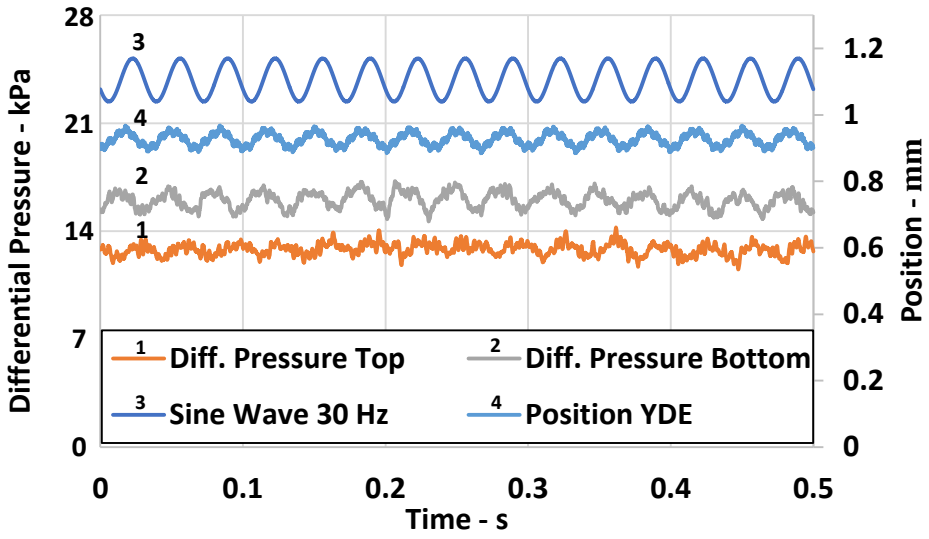

Figure 34. Position and pressure measurements vs time for 30 Hz precession at 3.79 bar inlet pressure and 0.7 pressure ratio.

Fourier analysis accurately determines the values of the variables needed to calculate the rotordynamic coefficients. Figure 35 shows typical results of Fourier analysis performed on data from all four position probes. The amplitude of the precession orbit is coordinated in a way that all axes have the same frequency response and amplitude. In this example, the peak displacement occurs at the precession frequency of 50 Hz. Another peak displacement belongs to the synchronous frequency 167 Hz, due to the rotor speed and imbalance. Other peaks occur at twice the synchronous speed of 333 Hz and an unexplained response at exactly 75 Hz.

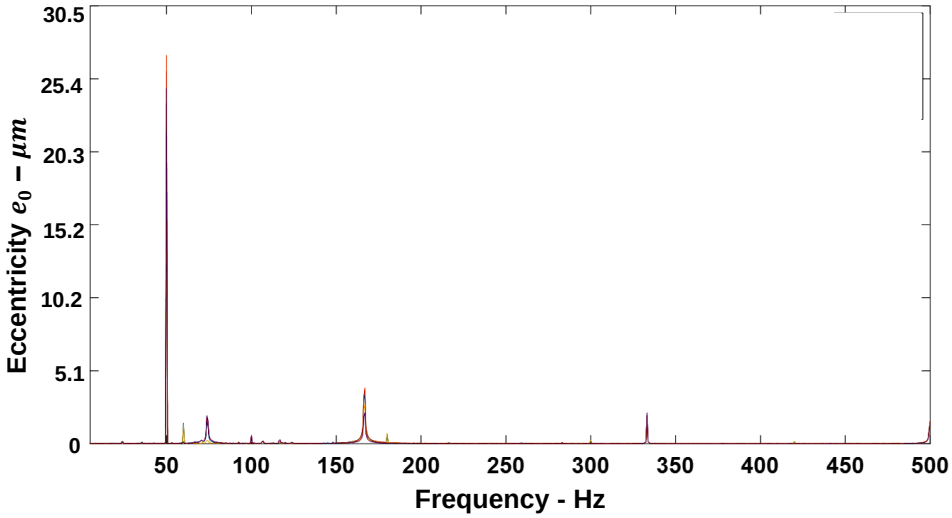

Figure 35. Frequency response position measurements for all axes for a 50 Hz precession at 3.79 bar inlet pressure and 0.7 pressure ratio.

Results of the Fourier analysis of the Top differential pressure transducer are shown in Fig. 36. A large response is seen at 50 Hz, corresponding to the precession frequency. Small peaks at 75 and 167 Hz correspond to vibration peaks shown in the previous figure. Clearly, the precession motion of the rotor has a direct impact on the dynamic pressure inside the seal.

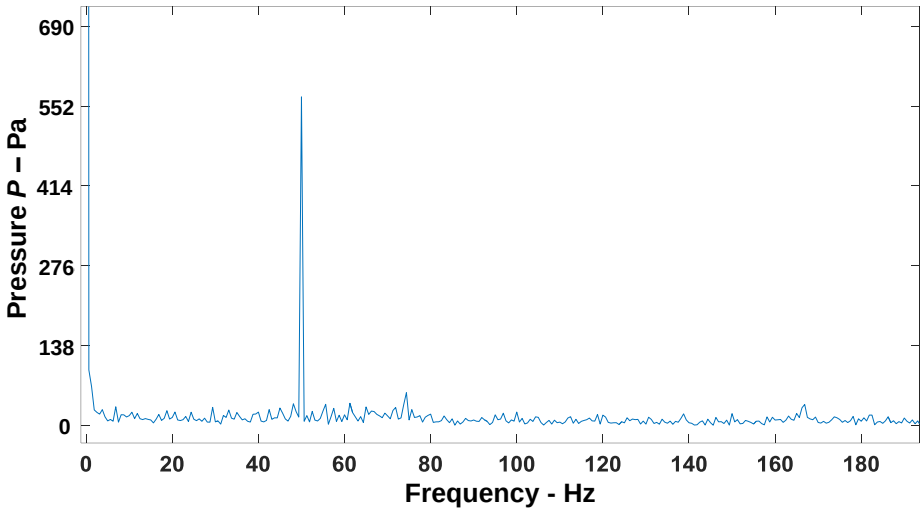

Figure 36. Frequency response of dynamic pressure sensor 6 for a 50 Hz precession at 3.79 bar inlet pressure and 0.7 pressure ratio

A coherence plot is useful in evaluating causality; How much is the pressure response due to the displacement of the rotor? Figure 37 is a coherence plot of the previous results. Values close to one suggest there is a direct correlation between the input position and the output pressure. A value close to one at 50 Hz suggests changing the rotor's position directly impacts the pressure inside the seal cavities. Similar time, frequency, and coherence responses are obtained for all tests.

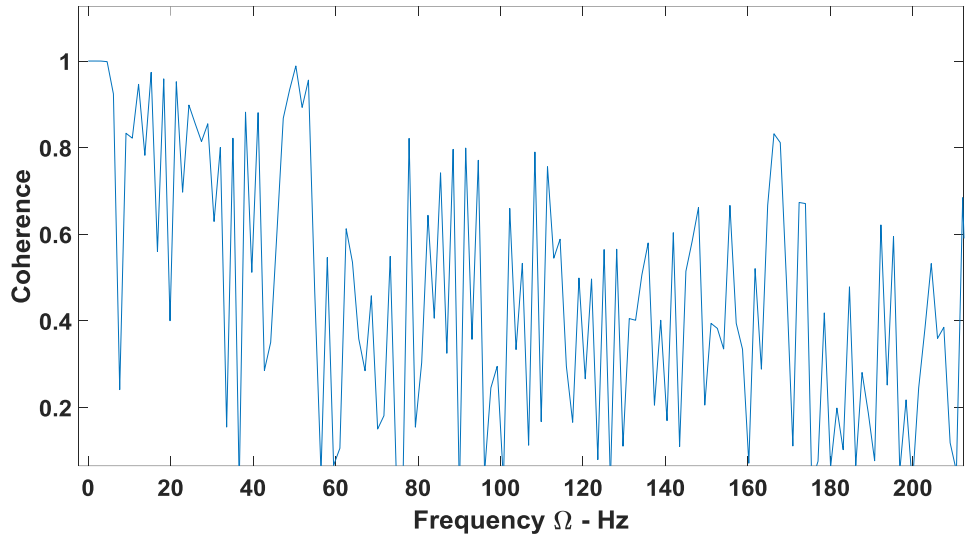

Figure 37. Coherence plot of output pressure due to an input displacement for a 50 Hz precession at 3.79 bar inlet pressure and 0.7 pressure ratio.

Figure 38 shows the pressure drop across each labyrinth cavity for tests at 10 kRPM. Linear curve fitting yields an average R^2 value of 0.985 for all tests suggesting an almost perfect linear drop in pressure across cavities. Uncertainty is small enough that error bars are barely visible in the graphs. Difficulty setting inlet pressures of 40, 55, and 4.83 bar result in lines crossing at the inlet.

(A)

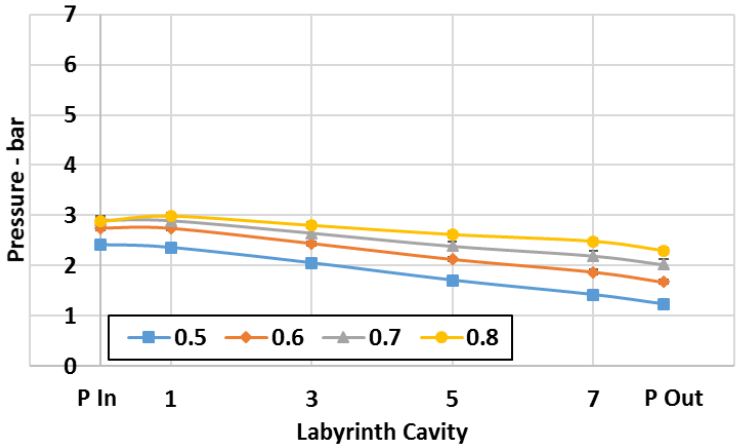

(B)

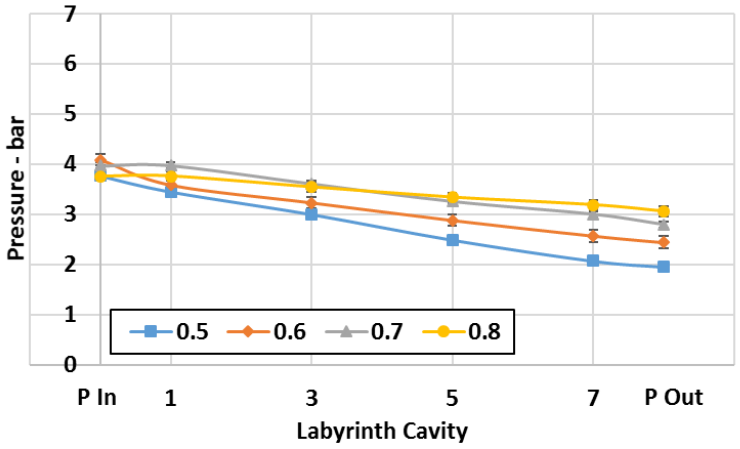

(C)

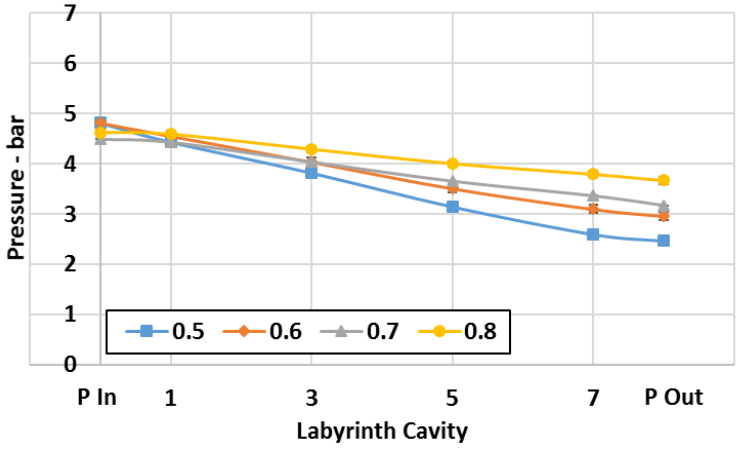

Figure 38. Pressure drop across labyrinth seal cavities for a (A) 2.76, (B) 3.79, and (C) 4.83 bar inlet pressure at 10 kRPM.

5. DYNAMIC RESULTS

The radial and circumferential forces measured in the third cavity are divided by e_0 and plotted vs precession frequency in Figs. 39 and 40. The rotordynamic coefficients are determined by the slope and intercept of a line of best fit through these points. Typically, the *y*-intercept of the graphs are the direct and cross-coupled stiffness terms, *K* and *k*, respectively. Similarly, the slope of each respective line is the cross-coupled and negative direct damping, *c* and -*C*. A linear best-fit outputs the rotordynamic coefficients, while its R^2 value determines the accuracy of the analysis.

Figure 39 shows test results of forward precessions at 3.79 bar inlet pressure and a 0.7 pressure ratio. Graphs (A) shows F_{r3}/e_0 versus Ω. From Eq. (7), for forward precession, $F_r/e_0 = K + c\Omega$. A best-fit dashed line through the data set yields the slope and intercept that translate into *K* and *c*. An R^2 value of 0.12 suggests a poor linear regression, due to the negligible influence of *c* in F_{r3}/e_0. The results are as expected, a small slope suggests negligible cross-coupled damping, and a negative *y*-intercept means *K* is negative as previously shown for *TOS* labyrinth seals by Arthur [5].

Figure 39 (B) shows $F_{\theta 3}/e_0$ versus Ω. Equation (8) states for forward precession, $F_\theta/e_0 = k - C\Omega$, thus a negative slope with a positive *y*-intercept as shown for $F_{\theta 3}/e_0$ refers to a positive *C* and positive *k*. An R^2 value higher than 0.9 demonstrates the accuracy of the measurements. Error bars given by uncertainty analysis are similar and acceptable in both graphs (A) and (B).

Figure 39 (C) shows β versus Ω for both differential pressure transducers. The phase is wrapped between 0 and 360 degrees for convenience. Clocking both phase measurements to the housing's *y*-axis for reference means that identical β values are in reality 180° apart from each other. As expected, measured phases between Top and Bottom sensors are 180° apart. The β values indicate a pressure wave that lags the rotor by more than 120°. A phase lag larger than 90° explains the negative direct stiffness forcing the rotor radially outward.

Figure 39 (D) shows pressure amplitude for the Top and Bottom differential transducers. Ideally the amplitudes would be equal, but for reasons unknown they are not. Improvements in stator alignment were key to achieve phase angles between the Top and Bottom transducers 180° from each other and comparable magnitudes. Results of β and pressure magnitude are obtained for all tests and shown in Appendix D.

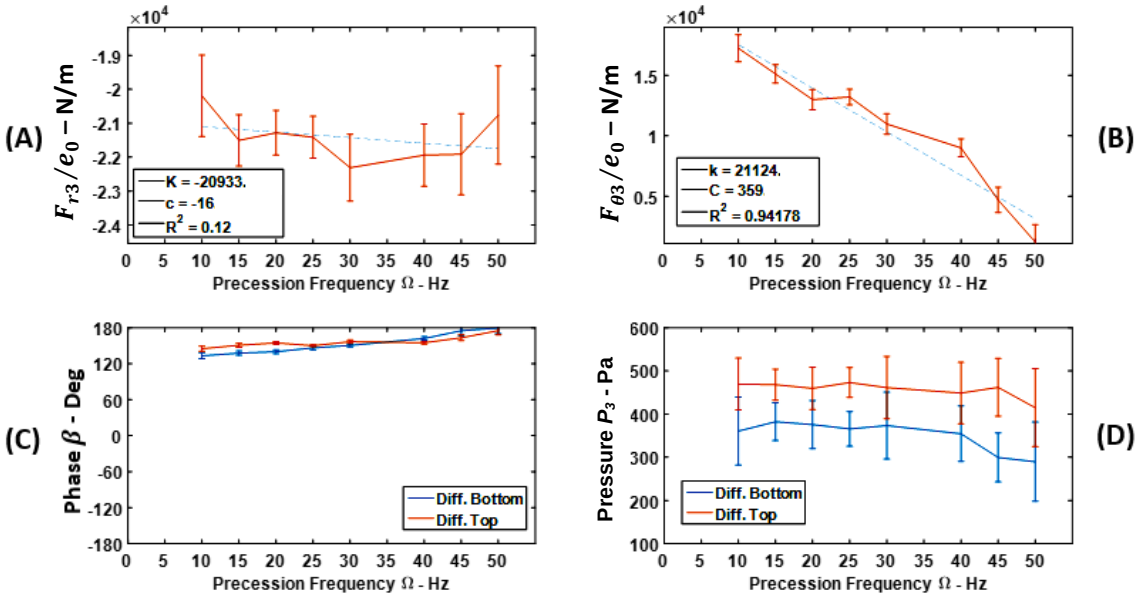

Figure 39. Measured (A) F_r/e_0 , (B) F_θ/e_0 , (C) β, and (D) P_3 for forward precession at 3.79 bar inlet pressure and 0.7 pressure ratio.

Figure 40. shows similar data for backward precession frequencies. Figure 40 (A) shows F_{r3}/e_0 versus Ω with an R^2 value of 0.98 indicating an excellent linear fit between different data points. The slope of F_{r3}/e_0 is inverted due to the negative precession frequencies. The results yield a negative *K*, and negligible *c*.

Figure 40 (B) shows $F_{\theta 3}/e_0$ versus Ω, with an inverted slope due to backward precession. An R^2 value of 0.96 reiterates the goodness of fit. The slope and *y*-intercept yield positive values of *C* and *k*.

Figure 40 (C) shows similar β measurements for the top and bottom differential pressure transducers, meaning the sensors are 180° apart from each other; once again P_3 lags e_{0r} by 120°, meaning the rotor is being pushed radially towards the seal (see Fig. 6).

In Fig. 40 (D), as in Fig. 39 (D), the magnitudes show a lower value for the Bottom differential pressure transducer than the Top one. The author believes that a (slightly) misaligned seal with larger clearances in the bottom creates differences in the magnitudes of the dynamic pressure. Similar results for backward precession are obtained for all tests and shown in Appendix D.

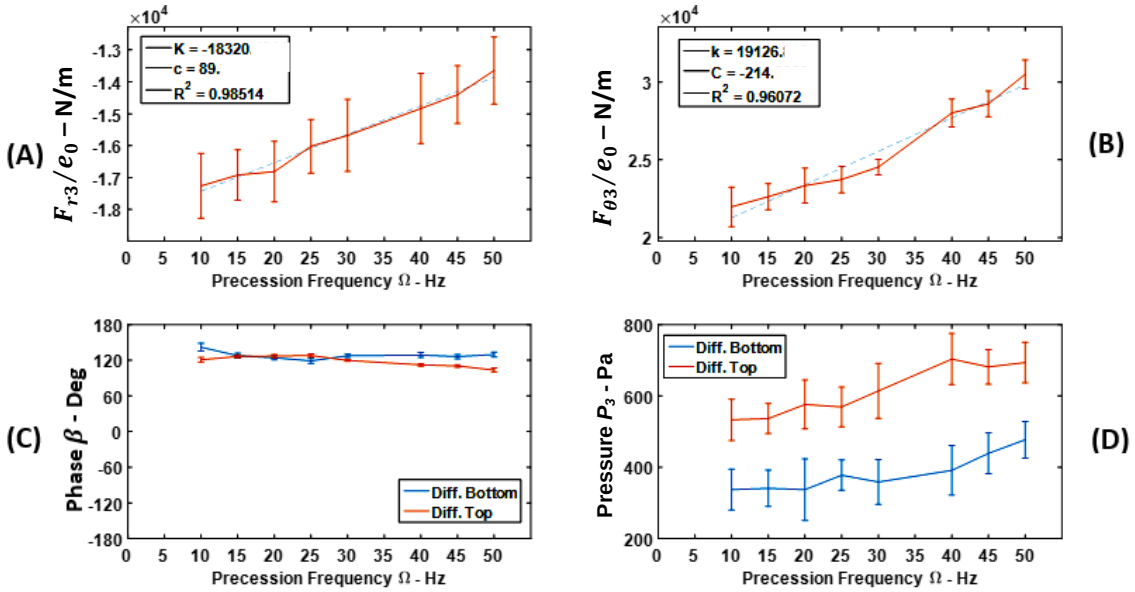

Figure 40. Measured (A) F_r/e_0 , (B) F_θ/e_0 , (C) β, and (D) P_3 for backward precession at 3.79 bar inlet pressure and 0.7 pressure ratio.

Figure 41 shows $F_{\theta 3}/e_0$ for all tests. Negative frequencies represent results obtained for backward precessions. Negative and positive frequencies form a straight line crossing the *y*-axis to show that the obtained rotordynamic coefficients are valid. The average R^2 value is 0.96, meaning there is an excellent linear trend between tests at backward and forward precessions. As expected, lower pressure ratios yield larger $F_{\theta 3}/e_0$ values due to larger pressure drops. All tests indicate positive *C* and *k* values.

Also expected is the increase in $F_{\theta 3}/e_0$ with increasing inlet pressure. Uncertainty values increase with increasing inlet pressure, and are especially bad at low precession frequencies at 4.83 bar inlet pressure. This may be due to test rig limitations.

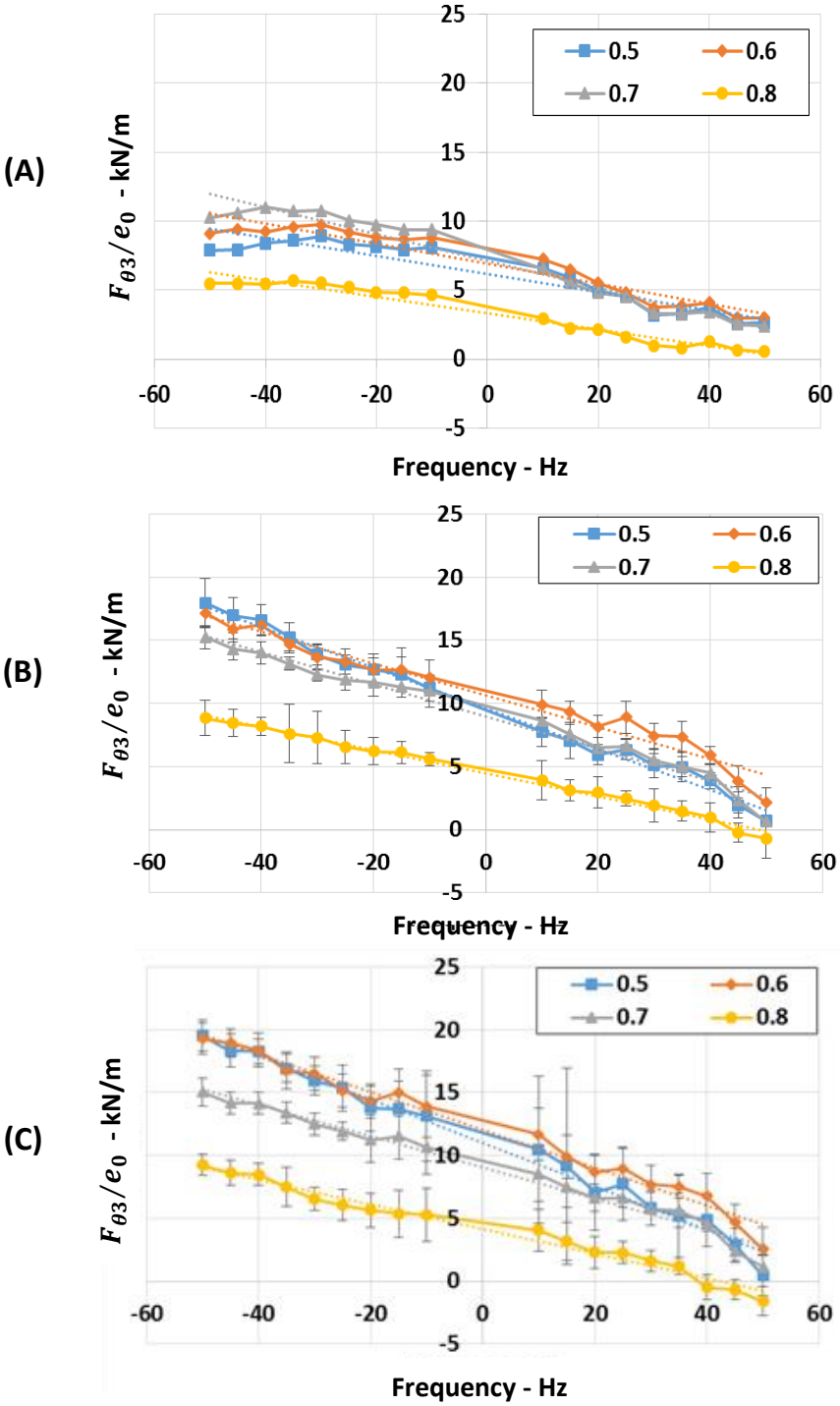

Figure 41. $F_{\theta 3}/e_0$ versus Ω for a (A) 2.76, (B) 3.79, and (C) 4.83 bar inlet pressure, and four pressure ratios at 10 kRPM.

Figure 42 shows results for F_{r3}/e_0. Similarly to $F_{\theta 3}/e_0$, tests for backward and forward precession frequencies form a line as expected. The average R^2 in this case is 0.78, noticeably lower than for circumferential forces. That outcome is due to the negligible values of *c* and the resulting uncertainty of the slope of the line. Low values of *c* are also shown by Arthur [5] and support the common practice of neglecting its impact on labyrinth seals. Direct stiffness, *K* is clearly defined in all cases. All values of *K* are negative, and the magnitude increases with decreasing pressure ratio (increasing pressure drop). These results indicate a decentering force in the radial direction that increases as the pressure drop across the seal increases. Arthur [5] also measured negative radial stiffness values for *TOS* labyrinth gas seals. Test rig limitations are visible as uncertainty increases with increasing inlet pressure, as well as the much smaller F_{r3}/e_0 values of tests at a 0.8 pressure ratio vs other pressure ratios.

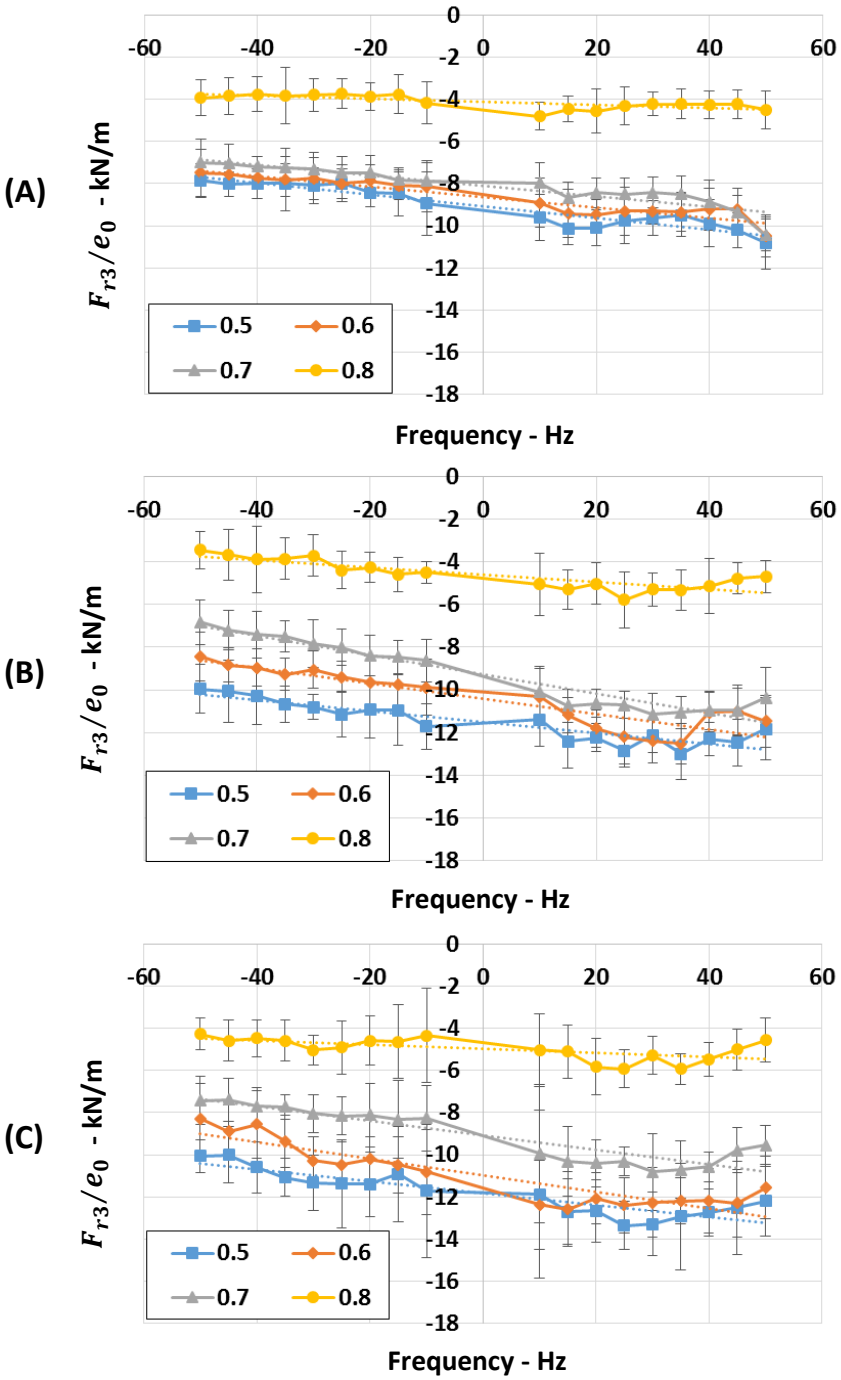

Figure 42. F_{r3}/e_0 versus Ω, for a (A) 2.76, (B) 3.79, and (C) 4.83 bar inlet pressure, and four pressure ratios at 10 kRPM.

Table 4 shows the rotordynamic coefficients obtained via slope and intercept as well as the goodness of fit of each linear regression. *C* is positive, thus stabilizing, it increases with decreasing pressure ratio, and with increasing inlet pressure. Cross-coupled stiffness *k* is positive and thus destabilizing, the influence of pressure ratio and inlet pressure is not so clear. The R^2 values suggest an excellent linear fit between tests. Cross-coupled damping is negative and small in magnitude, negative *c* is statically destabilizing as it pushes the rotor towards the seal. Direct stiffness *K* is negative for all cases. Its destabilizing effects increase with decreasing pressure ratio and increasing inlet pressure. R^2 values suggest a lower quality regression than circumferential force coefficients, because of negligible values of *c*. Another method to extract coefficients is presented below.

Table 4. Rotordynamic coefficients and R^2 values for linear regressions for third cavity.

kRPM	Inlet Pressure bar	Pressure Ratio	*C* kN-s/m	*k* kN/m	R^2	*c* kN-s/m	*K* kN/m	R^2
10	2.76	0.5	0.065	6.20	0.881	-0.028	-9.08	0.899
		0.6	0.073	6.90	0.919	-0.025	-8.61	0.897
		0.7	0.097	7.12	0.954	-0.025	-8.09	0.857
		0.8	0.059	3.35	0.954	-0.007	-4.12	0.548
	3.79	0.5	0.161	9.64	0.991	-0.026	-11.51	0.814
		0.6	0.126	10.63	0.961	-0.036	-10.40	0.819
		0.7	0.128	9.00	0.973	-0.046	-9.28	0.929
		0.8	0.092	4.48	0.992	-0.017	-4.59	0.714
	4.83	0.5	0.173	11.03	0.985	-0.028	-11.82	0.796
		0.6	0.151	12.04	0.979	-0.039	-10.96	0.820
		0.7	0.125	9.07	0.976	-0.035	-9.09	0.828
		0.8	0.099	4.14	0.977	-0.010	-4.97	0.400

Measurements of F_{r3}/e_0 and $F_{\theta 3}/e_0$ for forward and backward precessions are combined at each frequency using Eqs. (9-13) to extract rotordynamic coefficients as functions of frequency. Figure 43 shows *K* for all tests using this method. Constant lines across the range of frequencies demonstrate the frequency-independent nature of *TOS* labyrinth seals. The values of *K* are very similar to those obtained using a slope and intercept method. The uncertainty of the results increases substantially with increasing inlet pressure.

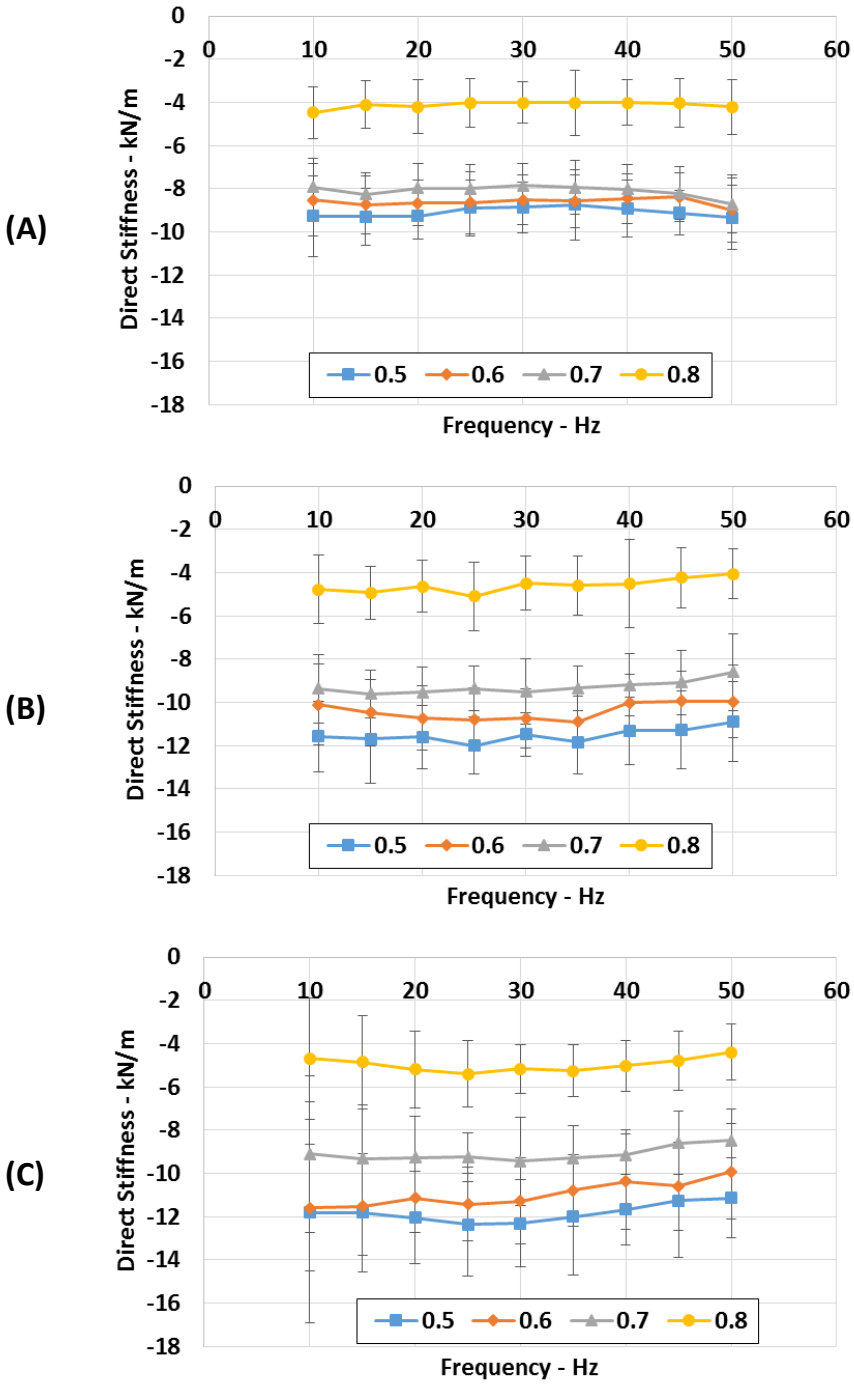

Figure 43. *K* versus Ω for third cavity for a (A) 2.76, (B) 3.79, and (C) 4.83 bar inlet pressure and four pressure ratios at 10 kRPM.

Figure 44 shows *C* for the third cavity for all tests obtained via backward-forward combined tests. Once again, constant lines suggest frequency independent coefficients. The values are very similar to those in Table 4. Large uncertainties occur at low frequencies and high inlet pressure due to the Kline McKlintock equations that in this case divide the uncertainty by the precession frequency.

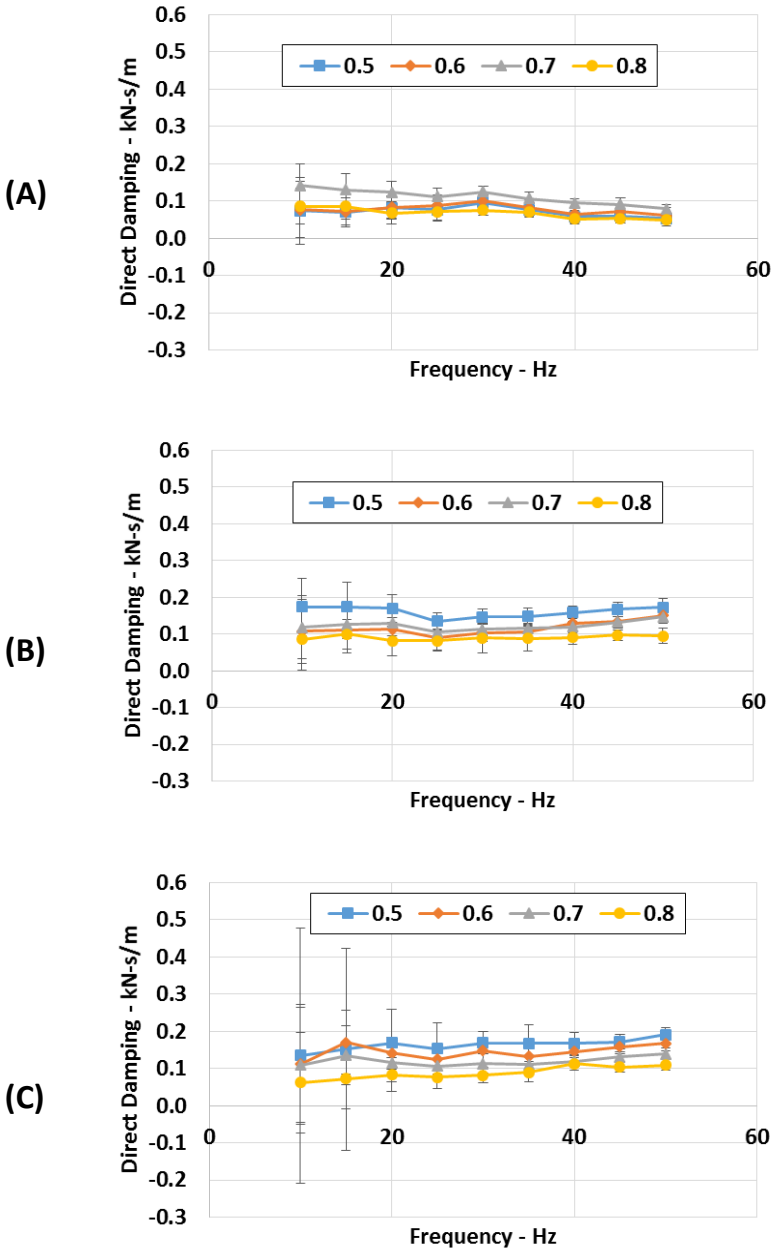

Figure 44. *C* versus Ω for third cavity for a (A) 2.76, (B) 3.79, and (C) 4.83 bar inlet pressure and four pressure ratios at 10 kRPM.

Figure 45 shows *k* versus Ω for the third cavity for all tests. The uncertainty increases with increasing inlet pressure.

(A)

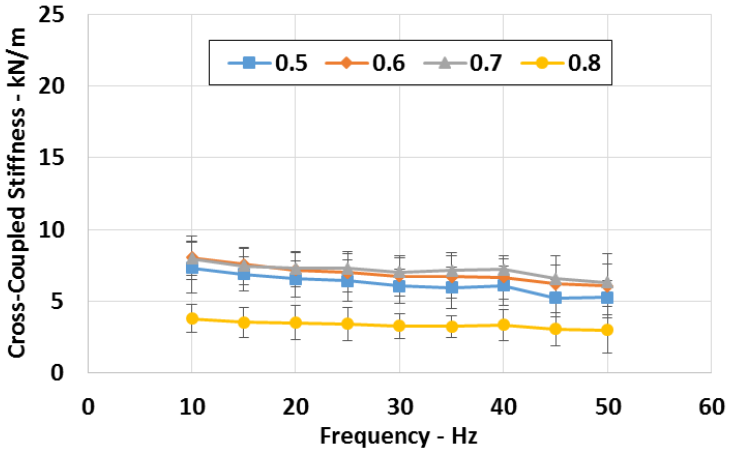

(B)

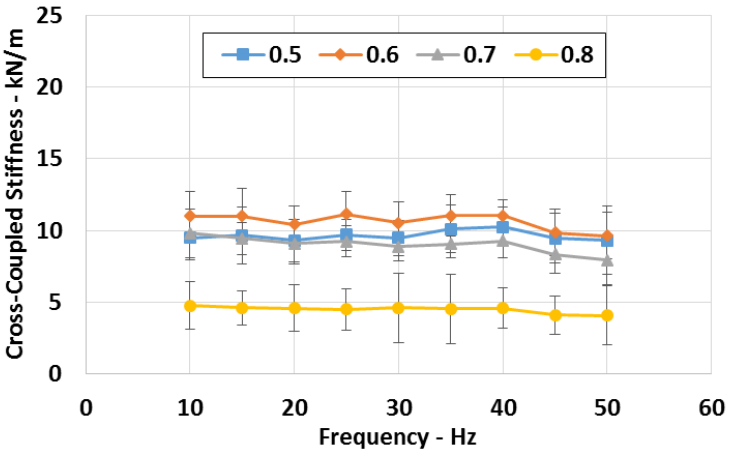

(C)

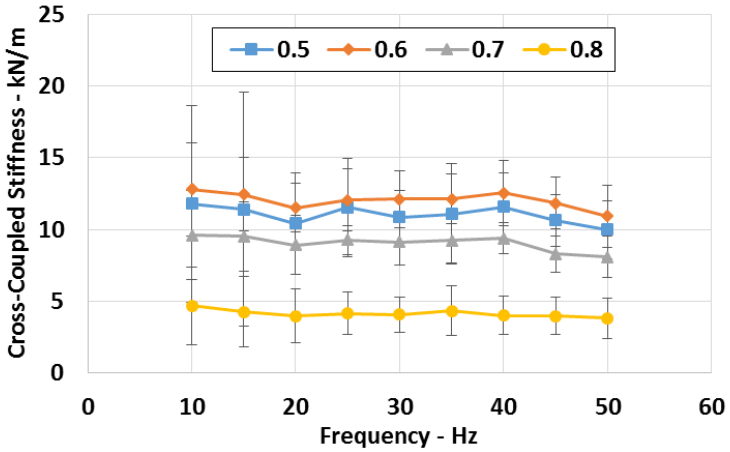

Figure 45. *k* versus Ω for third cavity for a (A) 2.76, (B) 3.79, and (C) 4.83 bar inlet pressure and four pressure ratios at 10 kRPM.

Figure 46 shows *c* versus Ω for the third cavity for all tests. As expected, the results are frequency independent and small in magnitude. Uncertainties at low frequencies are large due to Kline McKlintock calculations.

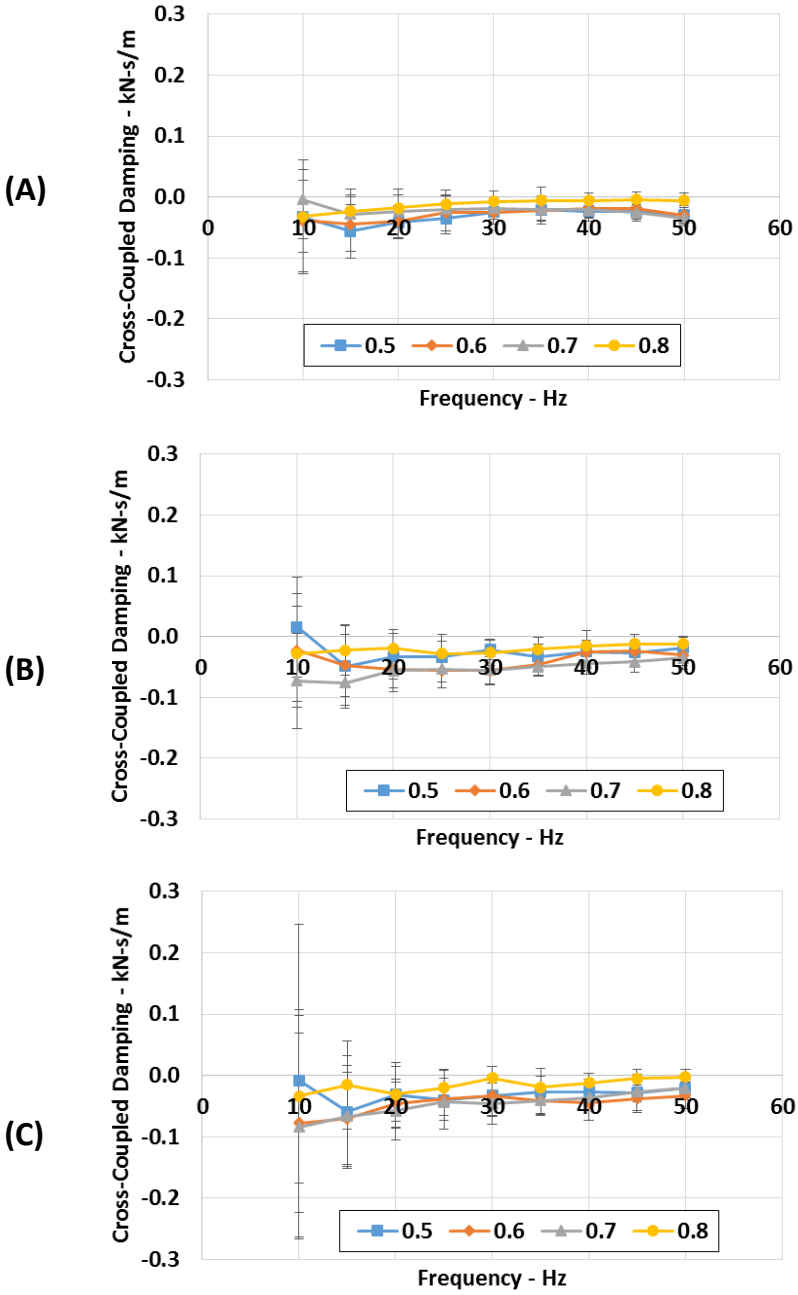

Figure 46. *c* versus Ω for third cavity for a (A) 2.76, (B) 3.79, and (C) 4.83 bar inlet pressure and four pressure ratios at 10 kRPM.

Effective Stiffness K_{eff} as defined in Eq. (6) accounts for the combined radial coefficients and is shown in Fig. 47 versus Ω. Data obtained by means of slope and *y*-intercept is herein named ideal due to its invariability. The dotted lines represent ideal

data values of K_{eff} substituting the values in Table 4 in Eq. (6). The continuous line represents K_{eff} values obtained by substituting the values in Fig 43 and Fig 46 for each precession frequency. This figure compares both methods. In most cases, K_{eff} matches the ideal value within the uncertainty. Negative K_{eff} suggests a destabilizing effect in the radial direction. This happens when the pressure wave lags the rotor by more than 90° and less than 270°.

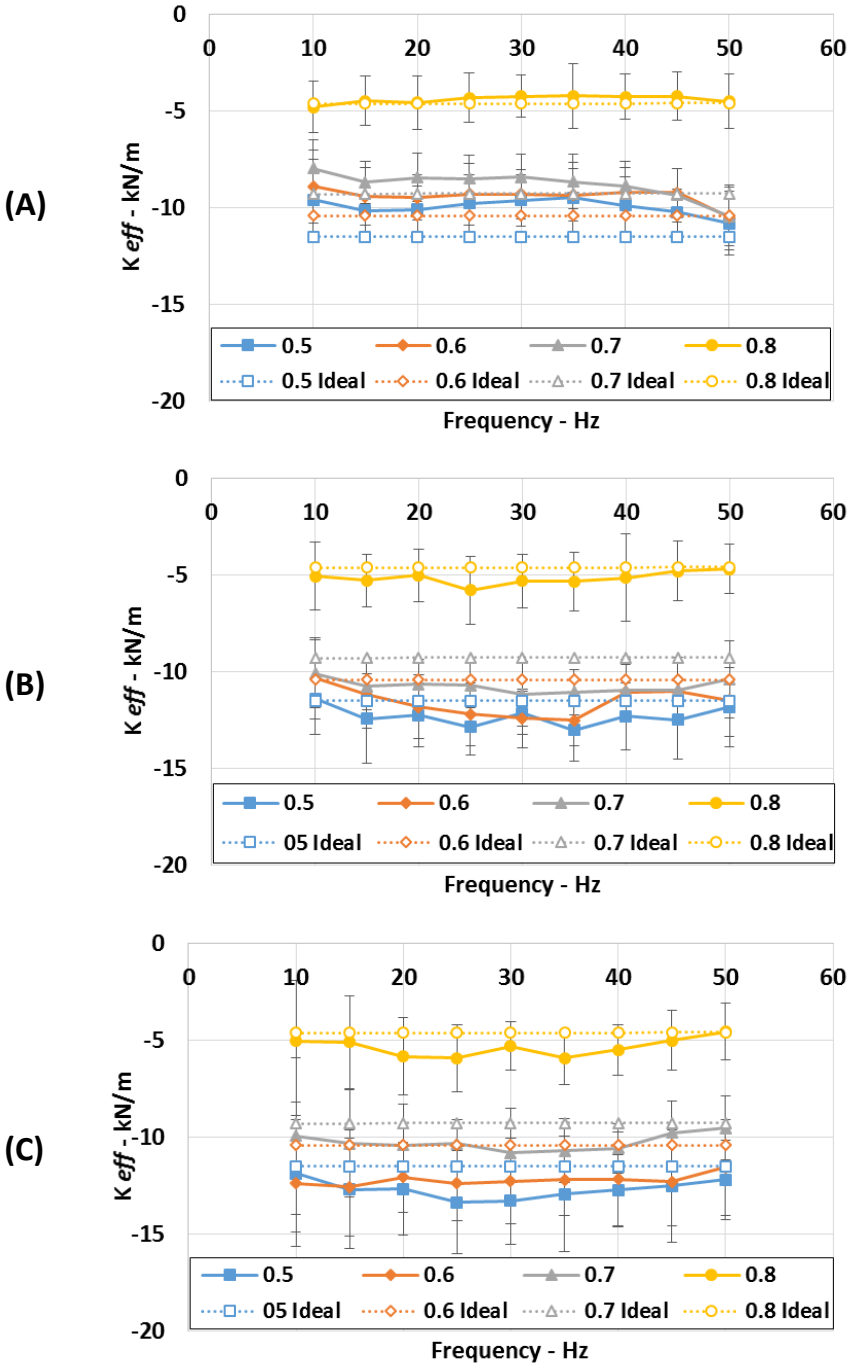

Figure 47. K_{eff} versus Ω for third cavity for a (A) 2.76, (B) 3.79, and (C) 4.83 bar inlet pressure and four pressure ratios at 10 kRPM.

C_{eff} as defined in Eq. (4) was obtained via two different methods is shown in Fig. 48. Data obtained by means of slope and *y*-intercept is herein named ideal due to its invariability. Continuous lines represent rotordynamic coefficients obtained via Eqs. (13-16). Results from both methods yield very similar results. The curvature is due to the division of k by Ω in Eq. (4). Uncertainty is low for all tests except at higher inlet pressures and lower frequencies. C_{eff} is negative although C is positive for all tests, because it is counteracted by a large positive k. The influence of increasing precession frequency in Eq. (4) decreases the negative value of C_{eff} and asymptotically reaches zero. The results suggest larger destabilizing effects at low precession frequencies in the circumferential direction.

(A)

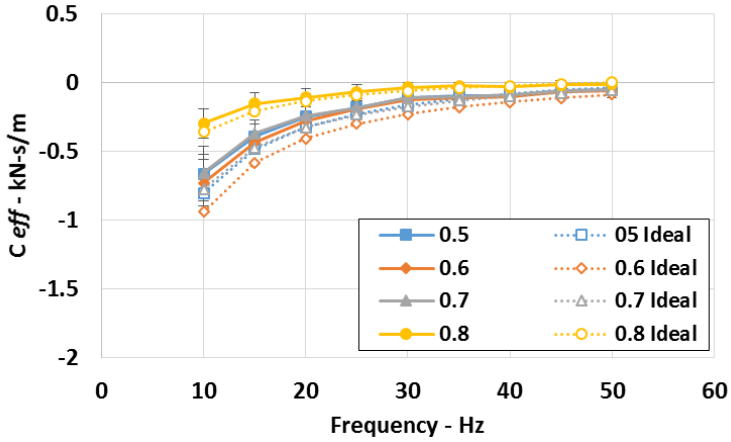

(B)

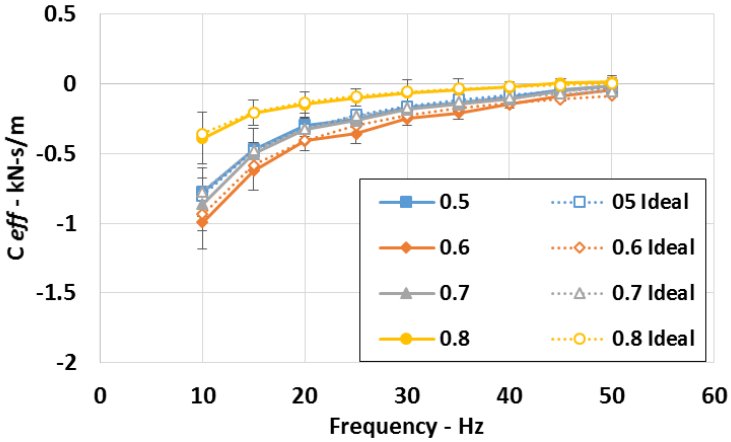

(C)

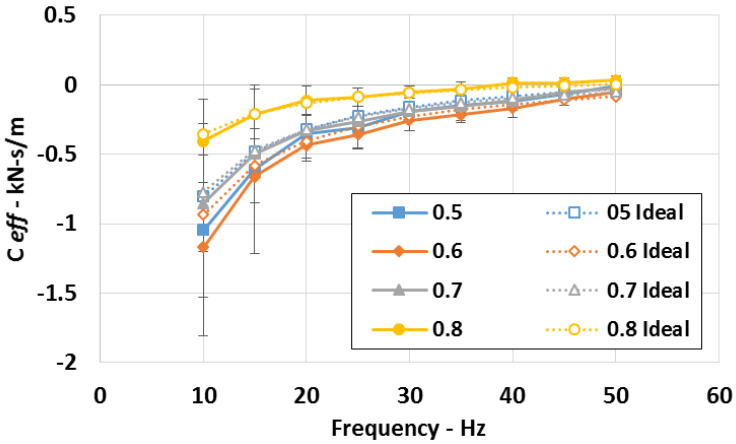

Figure 48. C_{eff} versus Ω for third cavity for a (A) 2.76, (B) 3.79, and (C) 4.83 bar inlet pressure and four pressure ratios at 10 kRPM.

WFR as defined in Eq. (5) was obtained for each frequency by combining backward and forward precession frequencies and is shown in Fig. 49. *WFR* decreases with increasing pressure ratio and remains constant for different inlet pressures. *WFR* is expected to resemble the *PSR* for *TOS* labyrinth seals. *WFR* measurements are between 0.05 and 0.1, an order of magnitude lower than the measured *PSR* values for a full labyrinth seal. To the writer's knowledge there are no prior *WFR* test results for one cavity of a *TOS* seal.

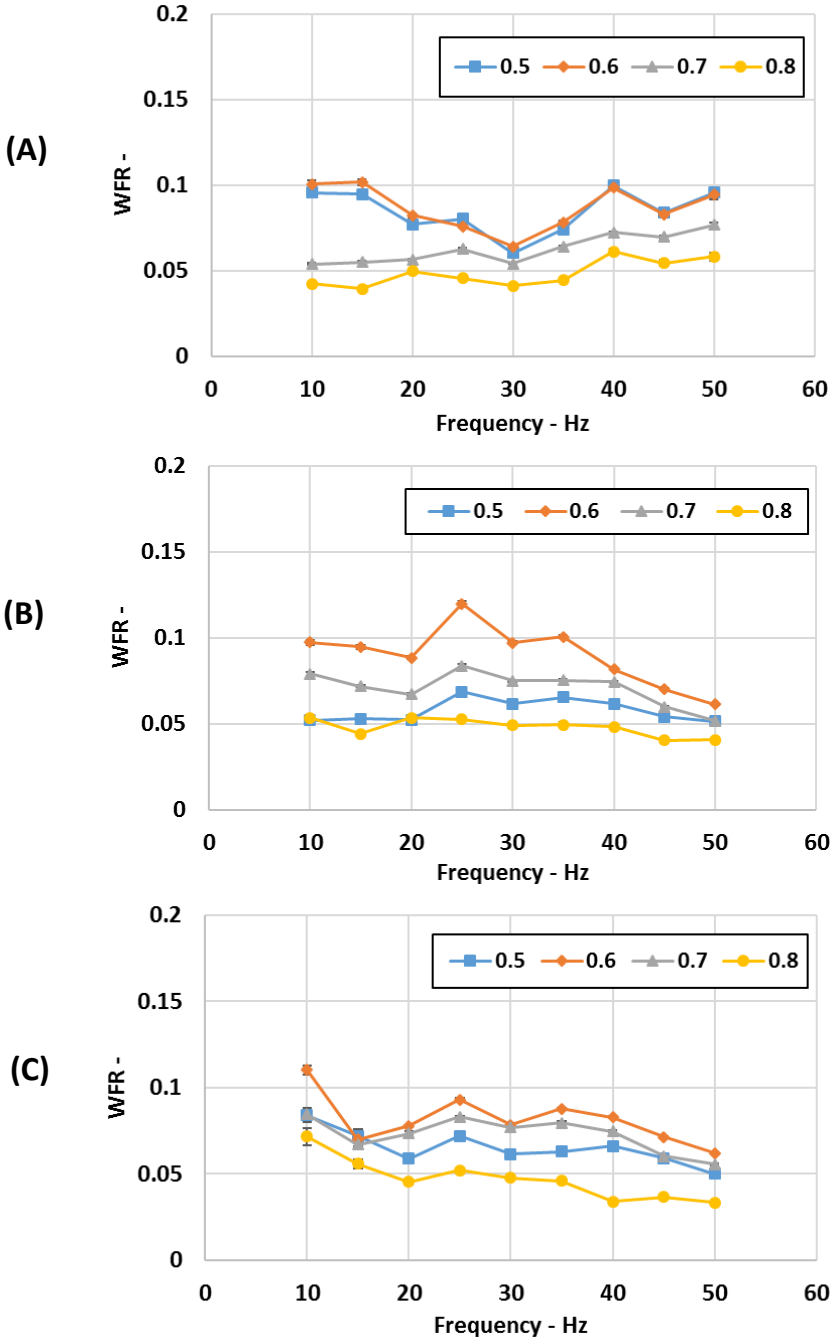

Figure 49. *WFR* versus Ω for third cavity for a (A) 2.76, (B) 3.79, and (C) 4.83 bar inlet pressure and four pressure ratios at 10 kRPM.

6. SUMMARY AND CONCLUSIONS

This work focuses on developing a test rig suitable for interlocking labyrinth seal tests. The test rig adapts to non-see through seals, and can test with and without swirl brakes, for a range of inlet pressures and pressure ratios. *PSR* may be modified using different swirl vanes. Measurements include: flowrate, inlet swirl velocity, pressure drop across labyrinth cavities, and dynamic pressure and position to extract rotordynamic coefficients.

The author encountered problems when using dynamic pressure sensors and changed to a differential pressure transducer method described by Millsaps which worked well. Reboring the housing and careful alignment was required to obtain useful measurements. Measurements of a *TOS* labyrinth seal validate the performance and usefulness of the test rig.

All results are repeatable. Static pressure drops linearly across the seal's cavities. Experimental results show frequency-independent rotordynamic coefficients. Two different models using backward and forward precession frequencies yield similar results. Test rig limitations are notable at large inlet pressures and large pressure ratios.

Negative values of K and c confirm the lagging pressure wave is behind the rotor, pushing it radially towards the stator. Positive values of k and C counteract each other in the circumferential direction, the former being destabilizing. C_{eff} calculations using both methods show negative values, and thus destabilizing results in the circumferential direction.

Future work with the test rig includes testing all cavities of an interlocking seal simultaneously, with and without swirl brakes, and for a range of *PSR*. The results obtained may be used to benchmark (currently non-existent) CFD code for non-see-through labyrinth seals.

REFERENCES

[1] Whalen, John K., Eduardo Alvarez, and Lester P. Palliser. "Thermoplastic Labyrinth Seals for Centrifugal Compressors." Thirty-Third Turbomachinery Symposium Preceedings (2004): 113-26. Web. 17 May 2016.

[2] San Andrés, L., "Notes 2 – modern lubrication theory" Tribology Group, Texas A&M University. Web 2009. Accessed January 2016.

[3] Williams, B. P., and R. D. Flack. "Calculation of Rotor Dynamic Coefficients for Labyrinth Seals." International Journal of Rotating Machinery 4.4 (1998), pp. 257-69. Web.

[4] Childs, D. W., and J. K. Scharrer. "Experimental Rotordynamic Coefficient Results for Teeth-On-Rotor and Teeth-On-Stator Labyrinth Gas Seals." Journal of Engineering for Gas Turbines and Power 108 (1986), pp. 599-604.

[5] Childs, D. W., (1993). "Turbomachinery Rotordynamics – Phenomena, Modeling and Analysis" New York, John Wiley & Sons.

[6] Arthur, S.P. (2015), "Measured Rotordynamic Coefficients and Leakage for a Tooth-On-Rotor Labyrinth Seal with Comparisons to a Tooth-On-Stator Labyrinth Seal," MS Thesis, Department of Mechanical Engineering, Texas A&M University, College Station.

[7] Benckert, H., and J. Wachter. "Flow Induced Spring Coefficients of Labyrinth Seals for Application in Rotor Dynamics." NASA Conference Publication 2133 (1980), pp. 189-212.

[8] Childs, D. W., David A. Elrod, and Keith Hale. "Rotordynamic Coefficient and Leakage Test Results for Interlock and Tooth-on-Stator Labyrinth Seals." ASME (1988), pp. 1-7. Web.

[9] Baumann, U. "Rotordynamic Stability Tests on High-Pressure Radial Compressors." Preceedings of the 28th Turbomachinery Symposium (1999), pp. 115-22. Web.

[10] Millsaps, K. T., and Martinez-Sanchez, M. (1994), "Dynamic Forces from Single Gland Labyrinth Seals: Part I – Ideal and Viscous Decomposition" Journal of Turbomachinery, ASME, Vol. 116, Oct. 1994, pp. 686-693.

[11] Wagner, N. G., Steff, K., Gausmann, R., & Schmidt, M. (2009). "Investigations on the Dynamic Coefficients of Impeller Eye Labyrinth Seals." Preceedings of the 38th Turbomachinery Symposium, pp. 53-70.

[12] Childs, D. W., "Reaction Force for a Rotor Precessing in a Two-Tooth/One-Cavity Labyrinth Seal in Terms of Perturbed Pressure." Texas A&M University Turbomachinery Lab, College Station, Tx, Personal Communication.

[13] Zutavern, Z. S. (2006), "Identification of Rotordynamic Forces in a Flexible Rotor System Using Magnetic Bearings." PhD Dissertation. Department of Mechanical Engineering, Texas A&M University, College Station.

[14] Gary, K. (2017), "Measurements of the Leakage and Rotordynamic Performance of Interlocking Labyrinth Seals." Master's Thesis. Department of Mechanical Engineering, Texas A&M University, College Station.

[15] Zutavern, Z. S. (2004), "Fiber Optic Strain Gauge Calibration and Dynamic Flexibility Transfer Function Identification in Magnetic Bearings" MS Thesis, Department of Mechanical Engineering, Texas A&M University, College Station.

APPENDIX A

DYNAMIC FORCE EQUATIONS BY CHILDS [12]

Reaction force for a rotor precessing in a two-tooth/one-cavity labyrinth seal in terms of perturbed pressure.

Assume that the rotor is precessing with an amplitude of e at a precession frequency of Ω. Assume that the peak pressure lags the rotating vector by the angle β. For e located by Ωt, the pressure distribution is

$$P(\theta) = P\cos(\theta - \Omega t + \beta) = P\cos\theta\cos(\beta - \Omega t) - P\sin\theta\sin(\beta - \Omega t)$$

If the axial length of the labyrinth chamber is L_c, the X and Y reaction forces are:

$$F_X = -L_c\int_0^{2\pi} P(\theta)\cos\theta R\,d\theta = -L_c PR\cos(\beta - \Omega t)\int_0^{2\pi}\cos^2\theta\,d\theta = -L_c PR\,\pi\cos(\beta - \Omega t)$$

$$F_Y = -L_c\int_0^{2\pi} P(\theta)\sin\theta R\,d\theta = L_c PR\sin(\beta - \Omega t)\int_0^{2\pi}\sin^2\theta\,d\theta = L_c PR\pi\sin(\beta - \Omega t)$$

These X-Y components are defined in terms of r-θ components via

$$\begin{Bmatrix} F_X \\ F_Y \end{Bmatrix} = \begin{bmatrix} \cos\Omega t & -\sin\Omega t \\ \sin\Omega t & \cos\Omega t \end{bmatrix} \begin{Bmatrix} F_r \\ F_\theta \end{Bmatrix} = \begin{bmatrix} \cos\Omega t & -\sin\Omega t \\ \sin\Omega t & \cos\Omega t \end{bmatrix} \begin{Bmatrix} -e(K + c\Omega) \\ e(k - C\Omega) \end{Bmatrix}$$

Equating the reaction force components gives

$$\begin{aligned} -L_c PR\pi\cos(\beta - \Omega t) &= -L_c PR\pi\cos\beta\cos\Omega t - L_c PR\pi\sin\beta\sin\Omega t \\ &= -e(K + c\Omega)\cos\Omega t - e(k - C\Omega)\sin\Omega t \end{aligned}$$

$$\begin{aligned} L_c PR\pi\sin(\beta - \Omega t) &= L_c PR\pi\sin\beta\cos\Omega t - L_c PR\pi\cos\beta\sin\Omega t \\ &= -e(K + c\Omega)\sin\Omega t + e(k - C\Omega)\cos\Omega t \end{aligned}$$

Equating $\cos\Omega t, \sin\Omega t$ terms from either equation produces

$$L_c R\pi(P\cos\beta) = e(K + c\Omega)\ ,\ L_c R\pi(P\sin\beta) = e(k - C\Omega) \qquad (1)$$

Starting with predicted values for K, k, C, c these equations can be used to determine the predicted pressure perturbations that will results from an orbit with amplitude e and precession frequency Ω.

From Eqs.(1), the perturbed pressure magnitude is

$$P = \frac{e\sqrt{(K + c\Omega)^2 + (k - C\Omega)^2}}{L_c R\pi} \tag{2}$$

The expected phase is

$$\beta = \tan^{-1}\left[\frac{(k - C\Omega)}{(K + c\Omega)}\right] \tag{3}$$

APPENDIX B

STATIC RESULTS AT 0 RPM

Table B - 1. Static conditions for tests at 0 RPM.

Inlet Pressure bar	Pressure Ratio	Inlet Pressure bar	Outlet Pressure bar	Pressure Ratio
2.76	0.5	2.68 ± 0.03	5.69 ± 0.02	0.502238
	0.6	2.83 ± 0.03	3.74 ± 0.13	0.607916
	0.7	2.81 ± 0.09	2.13 ± 0.02	0.687846
	0.8	3.04 ± 0.1	2.13 ± 0.02	0.796489
3.79	0.5	3.72 ± 0.1	5.71 ± 0.03	0.492189
	0.6	4.04 ± 0.03	2.46 ± 0.14	0.608517
	0.7	3.71 ± 0.07	2.60 ± 0.04	0.701699
	0.8	4.024 ± 0.11	3.21 ± 0.08	0.798543
4.83	0.5	4.69 ± 0.1	2.4 ± 0.07	0.506442
	0.6	4.75 ± 0.14	2.89 ± 0.10	0.608266
	0.7	4.85 ± 0.08	3.40 ± 0.06	0.702646
	0.8	5.02 ± 0.04	4.00 ± 0.04	0.797271

(A)

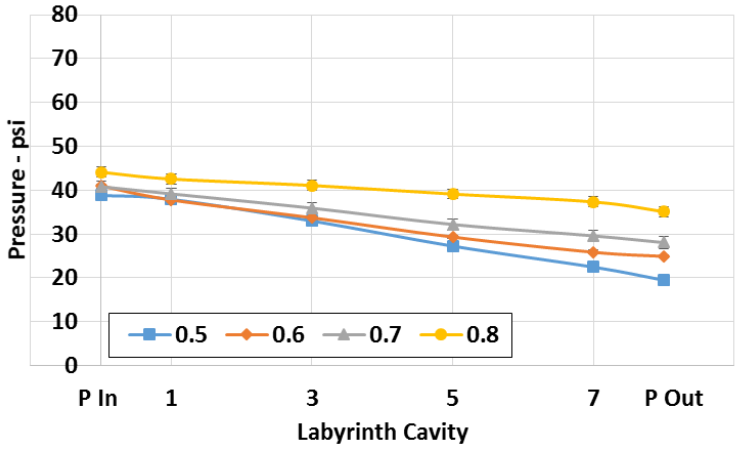

(B)

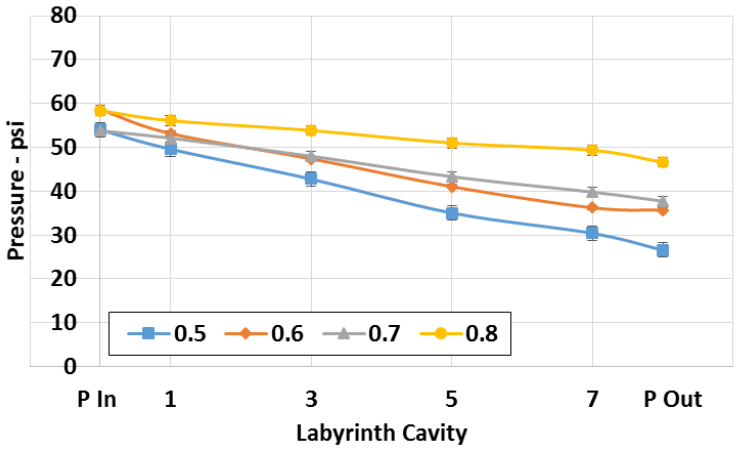

(C)

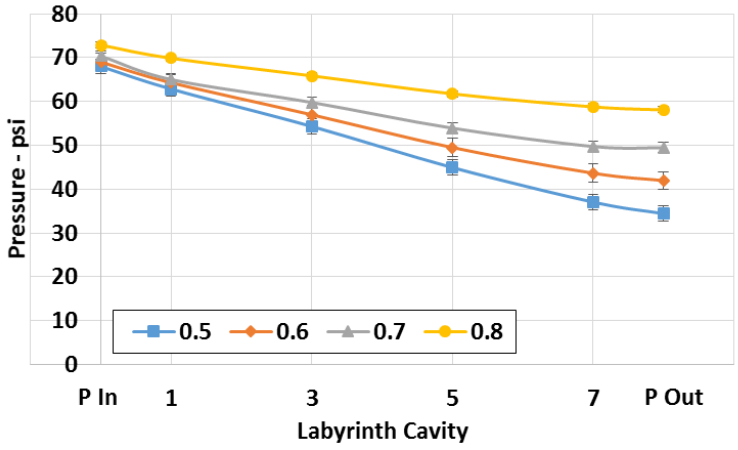

Figure B - 1. Pressure drop across cavities for a (A) 2.76, (B) 3.79, and (C) 4.83 bar inlet pressure at 0 RPM.

APPENDIX C

DYNAMIC RESULTS AT 0 RPM

(A)

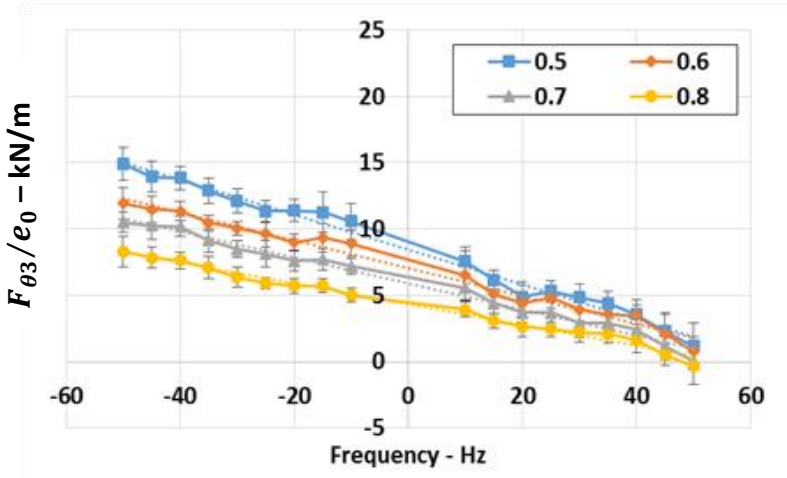

(B)

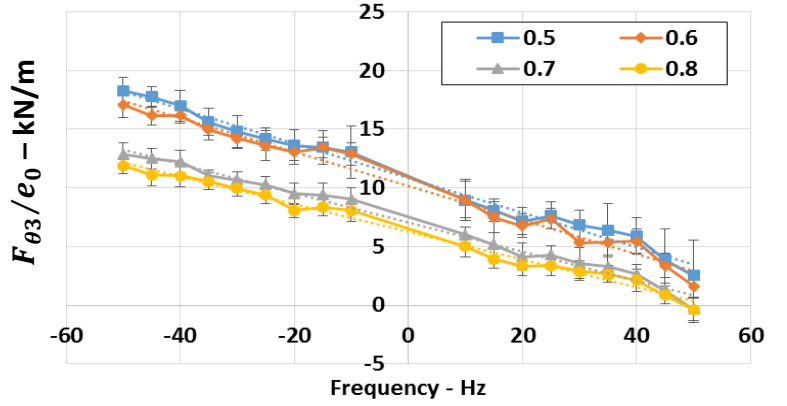

(C)

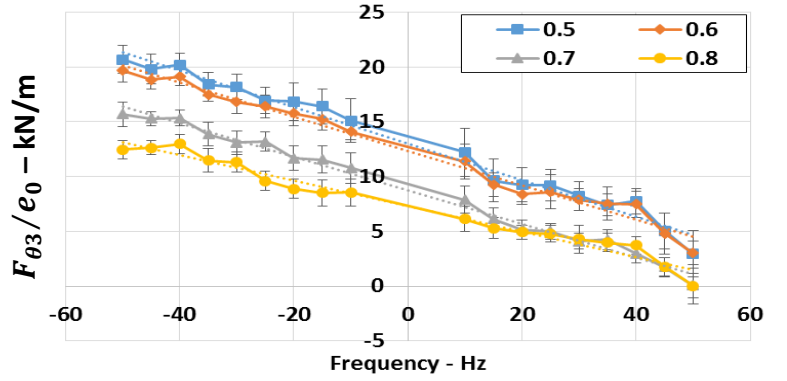

Figure B - 2. $F_{\theta 3}/e_0$ versus Ω for a (A) 2.76, (B) 3.79, and (C) 4.83 bar inlet pressure at 0 RPM.

(A)

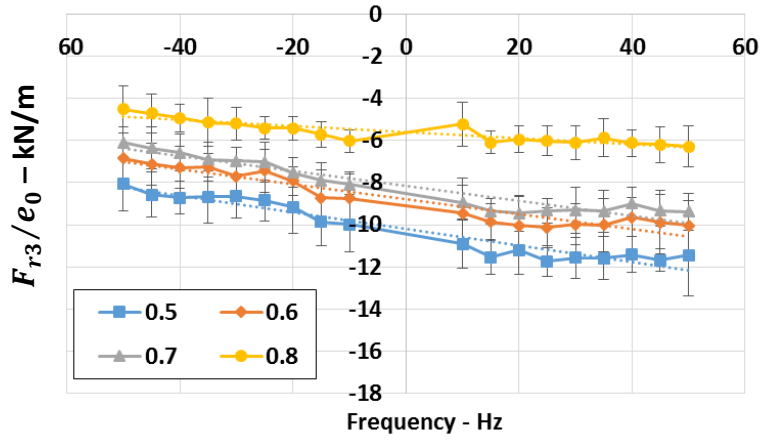

(B)

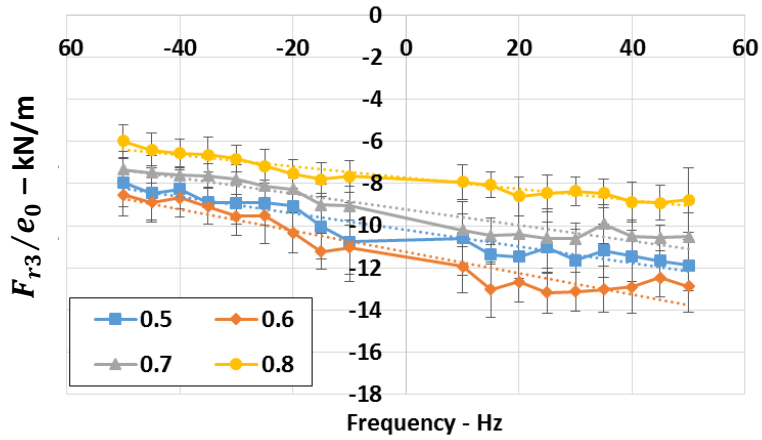

(C)

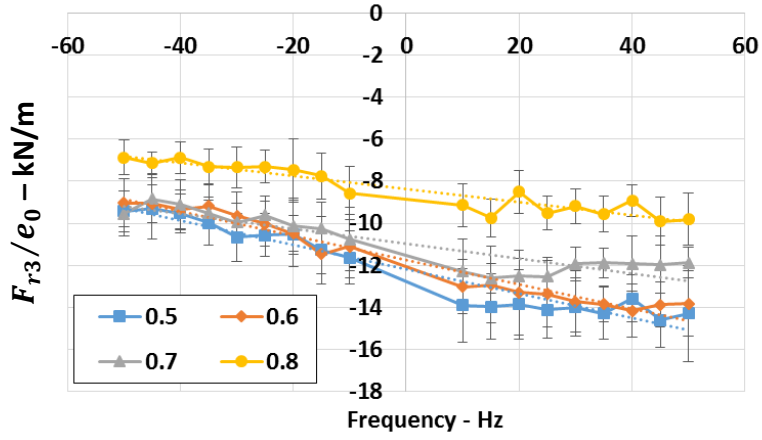

Figure B - 3. F_{r3}/e_0 versus Ω for a (A) 2.76, (B) 3.79, and (C) 4.83 bar inlet pressure at 0 RPM.

Table C - 1. Rotordynamic coefficients and R^2 values at 0 rpm.

kRPM	P In bar	Pressure Ratio	*C* kN-s/m	*k* kN/m	R^2	*c* kN-s/m	*K* kN/m	R^2
10	2.76	0.5	0.1315	8.476	0.9876	-0.0393	-10.199	0.927
		0.6	0.1053	7.049	0.982	-0.0352	-8.7845	0.9074
		0.7	0.0983	5.8895	0.9858	-0.03535	-8.158	0.9126
		0.8	0.07825	4.32375	0.9861	-0.01455	-5.6035	0.791
	3.79	0.5	0.1476	10.843	0.9878	-0.03915	-10.194	0.9168
		0.6	0.14535	10.187	0.9806	-0.05045	-11.224	0.9041
		0.7	0.1241	7.0825	0.9876	-0.03735	-9.2255	0.9108
		0.8	0.1179	6.2395	0.9887	-0.0268	-7.718	0.9375
	4.83	0.5	0.1671	13.014	0.982	-0.05805	-12.1975	0.9319
		0.6	0.15665	12.3255	0.9833	-0.0581	-11.745	0.961
		0.7	0.1531	8.761	0.9898	-0.0356	-10.9625	0.8095
		0.8	0.1161	7.2935	0.9725	-0.03125	-8.3805	0.881

APPENDIX D

DYNAMIC MEASUREMENTS

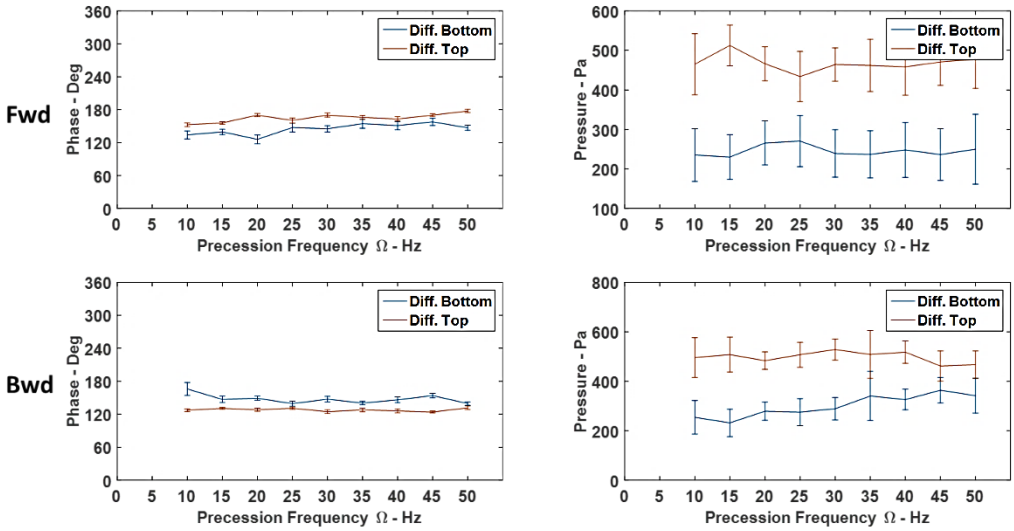

Figure D - 1 Phase *β* and pressure *P* of third cavity for 2.76 bar pressure drop at 0.5 PR.

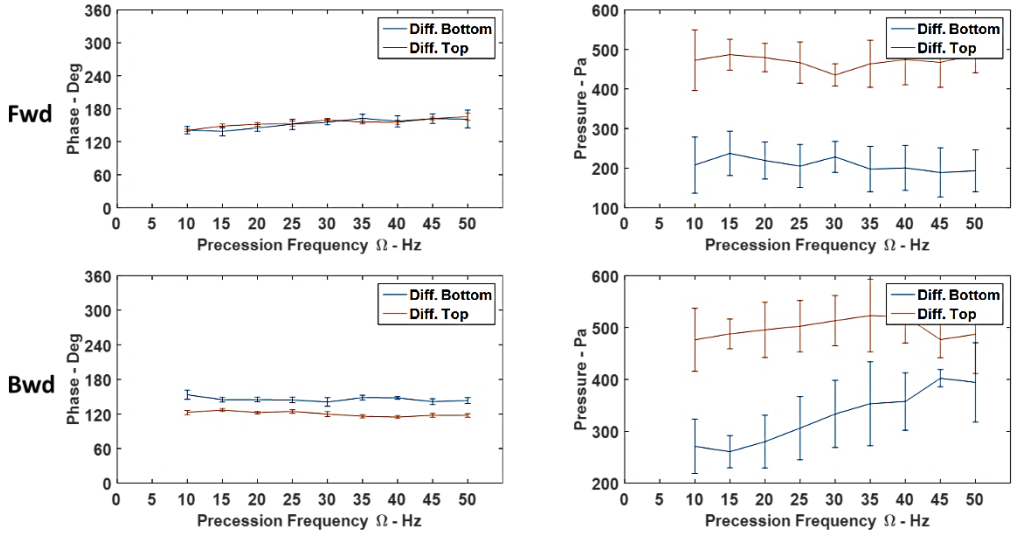

Figure D - 2 Phase *β* and pressure *P* of third cavity for 2.76 bar pressure drop at 0.6 PR.

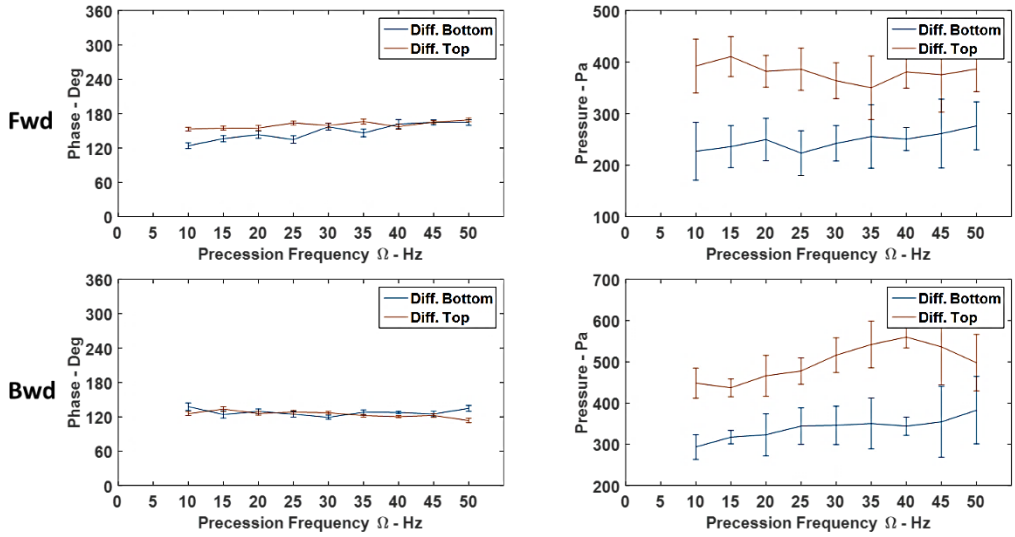

Figure D - 3 Phase *β* and pressure *P* of third cavity for 2.76 bar pressure drop at 0.7 PR.

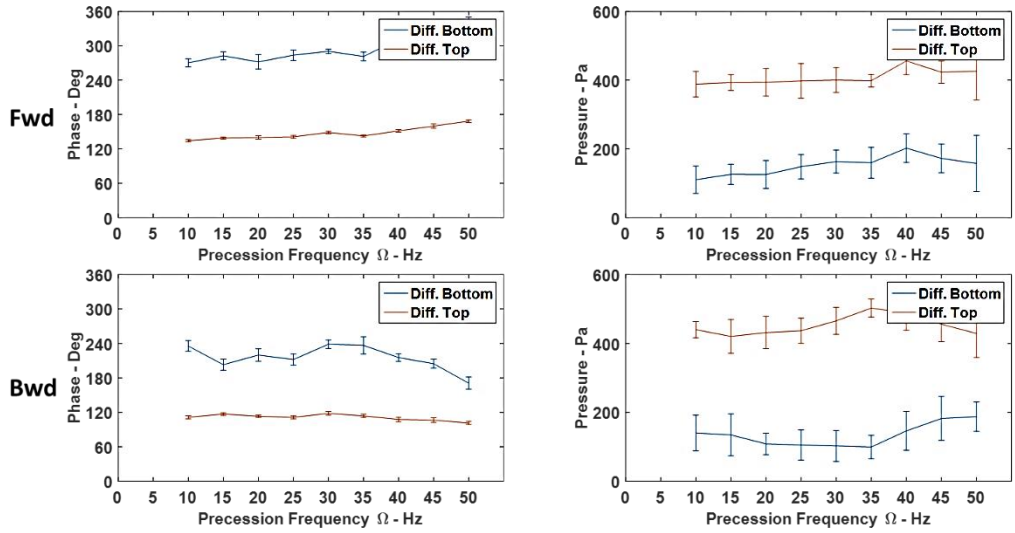

Figure D - 4 Phase *β* and pressure *P* of third cavity for 2.76 bar pressure drop at 0.8 PR.

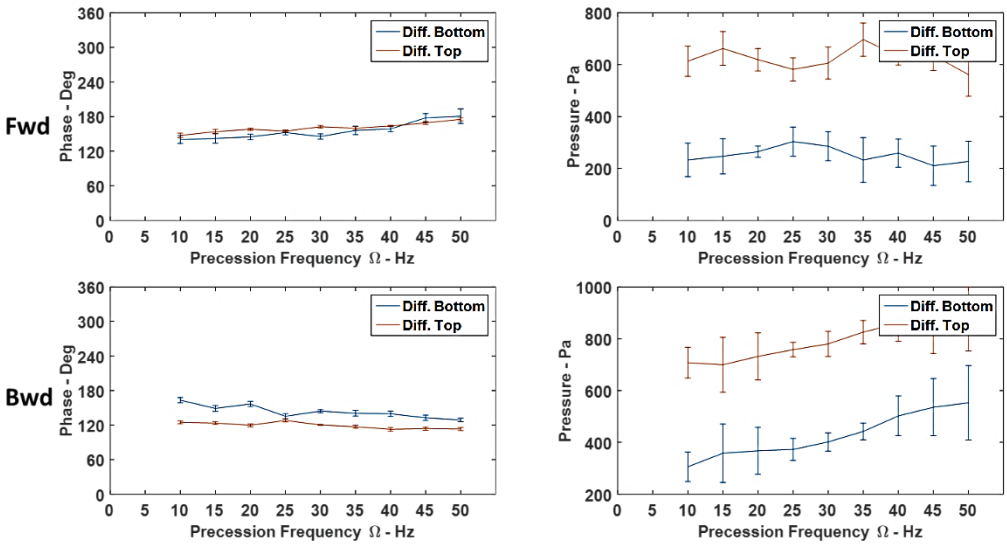

Figure D - 5 Phase *β* and pressure *P* of third cavity for 3.79 bar pressure drop at 0.5 PR.

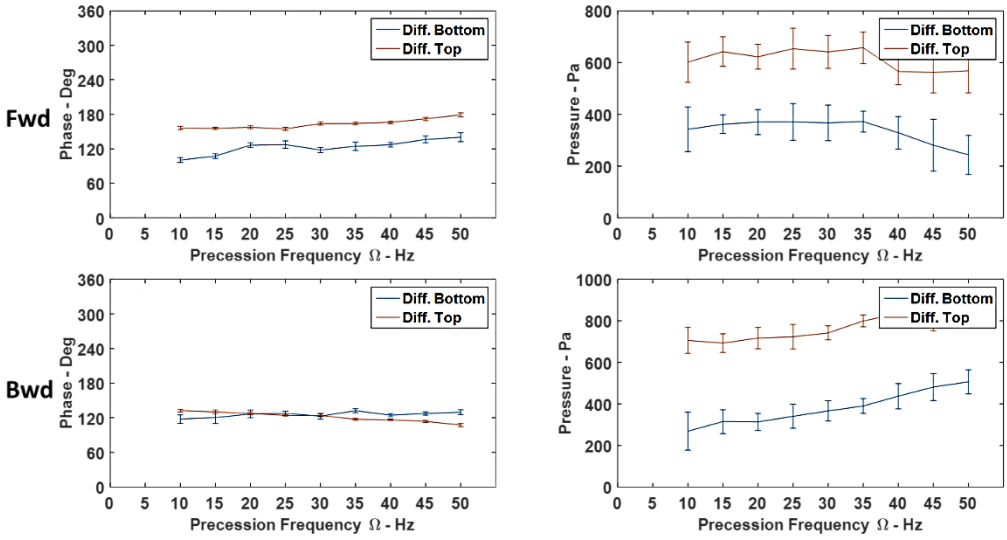

Figure D - 6 Phase *β* and pressure *P* of third cavity for 3.79 bar pressure drop at 0.6 PR.

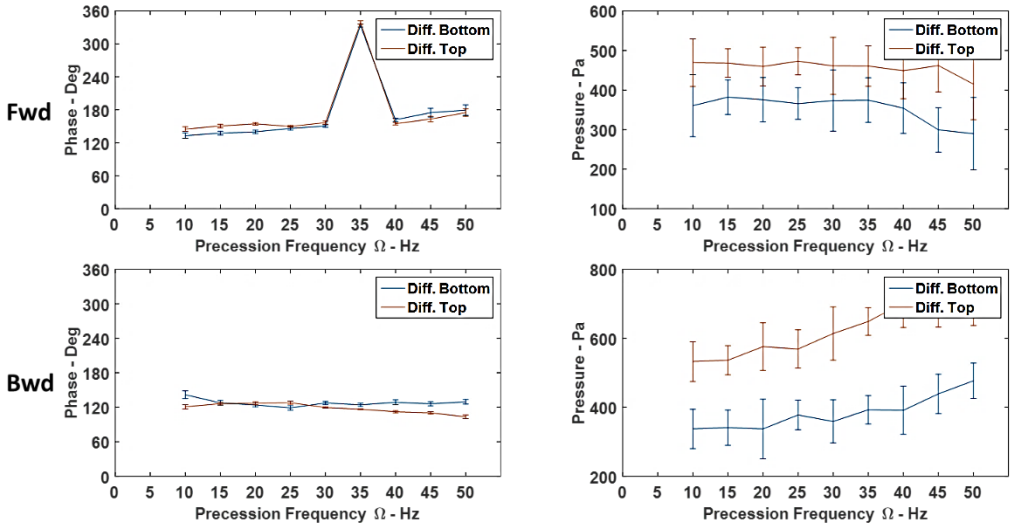

Figure D - 7 Phase *β* and pressure *P* of third cavity for 3.79 bar pressure drop at 0.7 PR.

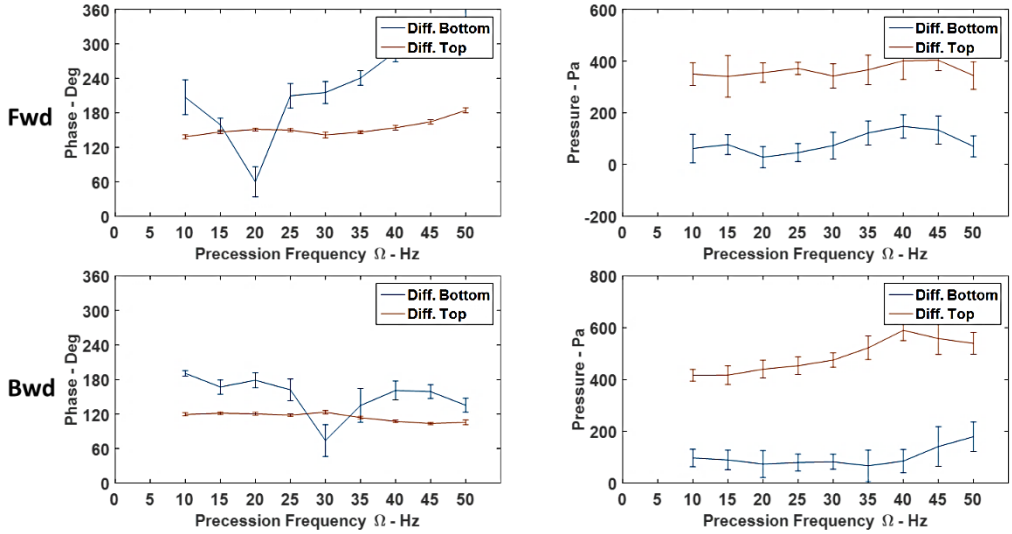

Figure D - 8 Phase *β* and pressure *P* of third cavity for 3.79 bar pressure drop at 0.8 PR.

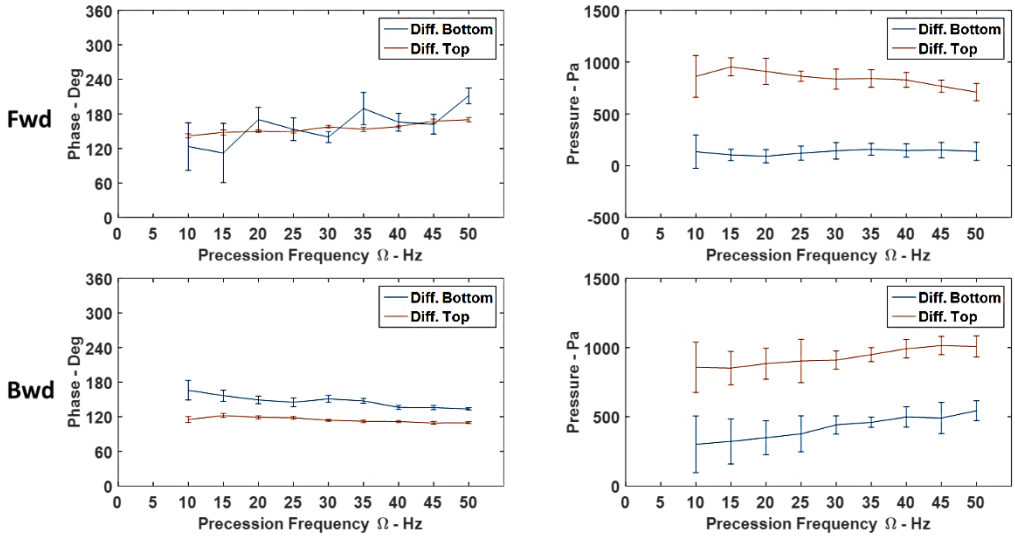

Figure D - 9 Phase *β* and pressure *P* of third cavity for 4.83 bar pressure drop at 0.5 PR.

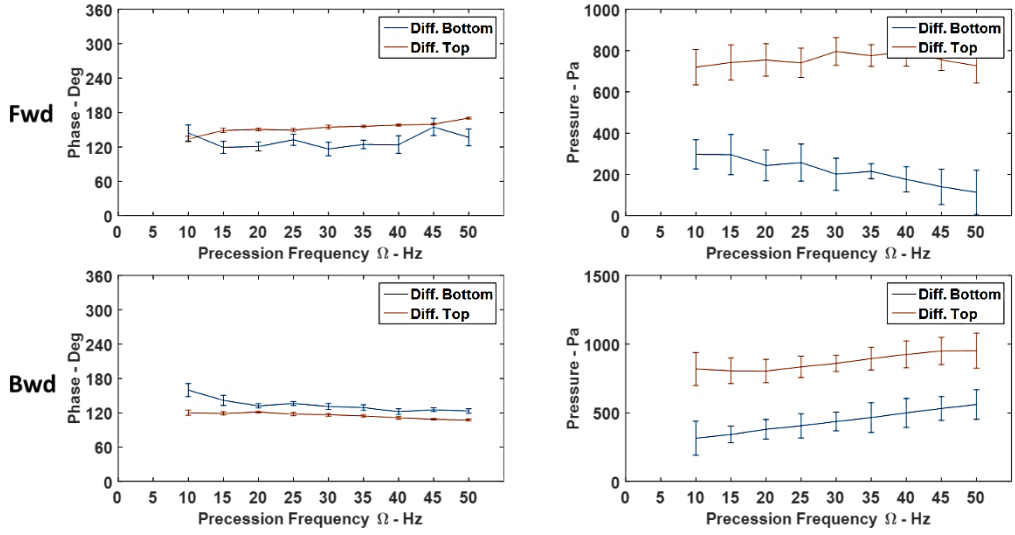

Figure D - 10 Phase *β* and pressure *P* of third cavity for 4.83 bar pressure drop at 0.6 PR.

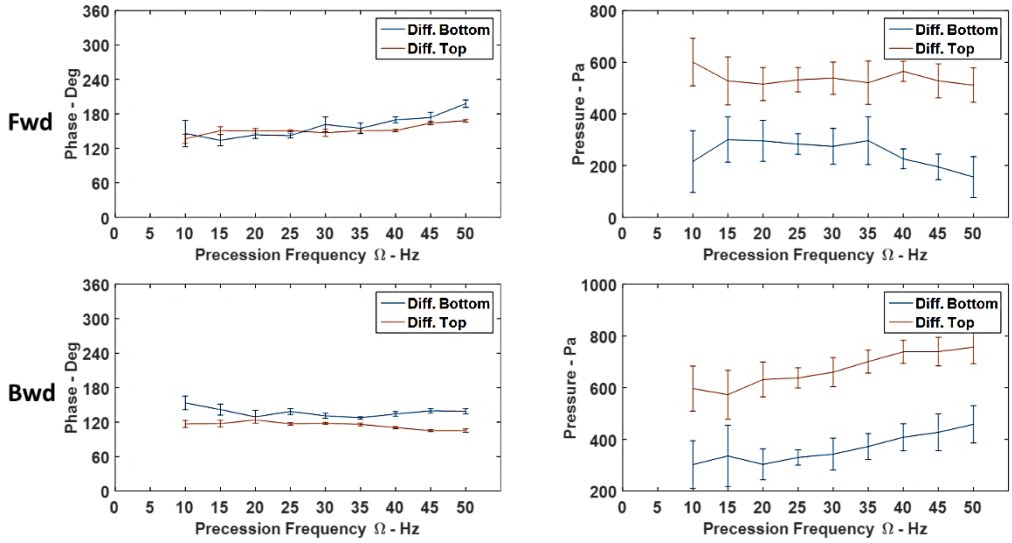

Figure D - 11 Phase β and pressure P of third cavity for 4.83 bar pressure drop at 0.7 PR.

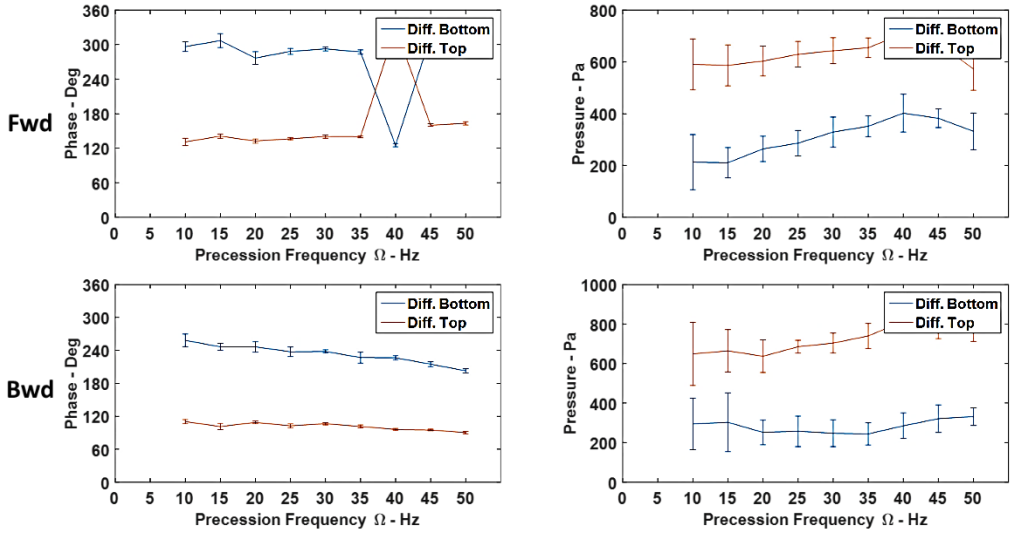

Figure D - 12 Phase β and pressure P of third cavity for 4.83 bar pressure drop at 0.8 PR.